Summer 2001

Geology of the Cooper Mountain Pluton, North Cascade Mountains, Washington Based on Magnetic Fabrics, Magnetic Remanence and Petrography

Tammy C. Fawcett
Western Washington University

GEOLOGY OF THE COOPER MOUNTAIN PLUTON, NORTH CASCADE MOUNTAINS, WASHINGTON BASED ON MAGNETIC FABRICS, MAGNETIC REMANENCE AND PETROGRAPHY

BY

Tammy C. Fawcett

Accepted in Partial Completion

of the Requirements for the Degree

Master of Science

Moheb A. Ghali, Dean of Graduate School

ADVISORY COMMITTEE

Chair, Dr. Bernard A. Housen

Dr. Susan M. DeBari

Dr. Edwin H. Brown

MASTER'S THESIS

In presenting this thesis in partial fulfillment of the requirements for a master's degree at Western Washington University, I agree that the Library shall make its copies freely available for inspection. I further agree that extensive copying of this thesis is allowable only for scholarly purposes. It is understood, however, that any copying or publication of this thesis for commercial purposes, or for financial gain, shall not be allowed without my written permission.

Signature _____

Date 7/27/2001

MASTER'S THESIS

In presenting this thesis in partial fulfillment of the requirements for a master's degree at Western Washington University, I grant to Western Washington University the non-exclusive royalty-free right to archive, reproduce, distribute, and display the thesis in any and all forms, including electronic format, via any digital library mechanisms maintained by WWU.

I represent and warrant this is my original work and does not infringe or violate any rights of others. I warrant that I have obtained written permissions from the owner of any third party copyrighted material included in these files.

I acknowledge that I retain ownership rights to the copyright of this work, including but not limited to the right to use all or part of this work in future works, such as articles or books.

Library users are granted permission for individual, research and non-commercial reproduction of this work for educational purposes only. Any further digital posting of this document requires specific permission from the author.

Any copying or publication of this thesis for commercial purposes, or for financial gain, is not allowed without my written permission.

Name: Tammy C. Fawcett

Signature: _____

Date: 7/16/2018

GEOLOGY OF THE COOPER MOUNTAIN PLUTON, NORTH CASCADE MOUNTAINS, WASHINGTON BASED ON MAGNETIC FABRICS, MAGNETIC REMANENCE AND PETROGRAPHY

A Thesis
Presented to the Faculty of
Western Washington University

In Partial Fulfillment
Of the Requirements for the Degree
Master of Science

By
Tammy C. Fawcett
July 2001

ABSTRACT

A study of the 48 Ma Cooper Mountain pluton (CMP) in the North Cascade Mountains of Washington using anisotropy of magnetic susceptibility (AMS) defined the orientation of magnetic fabrics. Fabrics in limited areas at the margins of the CMP tend to be parallel to the pluton margin and are therefore interpreted to be emplacement-related. The fabrics in the interior of the body, throughout the bulk of the pluton, are discordant with respect to the NW pluton margin. The fabric is manifest by NW-striking, moderately to steeply dipping foliation and NW-SE trending, moderately to shallowly plunging lineation, approximately parallel to regional structural trends in the Cascade Crystalline Core. Discordance of the fabric to the pluton margin and near concordance with regional structures suggests a tectonic origin.

Remanent magnetization was measured to determine if the CMP has been reoriented since emplacement. The characteristic remanence was unblocked in some samples at 580°C and in others at 370°C. A variety of techniques were used to determine that magnetite and pyrrhotite are the remanence-carrying minerals. Magnetic directions obtained from both of these remanence carriers plot, within error, on the North American expected Eocene direction (Diehl et al. 1983) suggesting that there has been no reorientation of the pluton since remanence was acquired and that magnetic fabrics require no correction to obtain their Eocene orientation.

Results of fabric analysis indicate that the Cooper Mountain pluton is a syn-tectonic pluton rather than post-tectonic (Haugerud et al. 1991b) due to the tectonic development of magmatic fabrics. This fabric is slightly oblique to the length of the

Cascade orogen and is thus best interpreted to have formed as a consequence of regional dextral-shear due to transpression.

ACKNOWLEDGEMENTS

First and foremost, I'd like to thank Bernie Housen, Russ Burmester and Myrl Beck for frequent encouragement, insight and paleomagnetic discussion. A huge debt of gratitude goes to Russ Burmester for all of his work running extra samples in the lab and for his endless answers to my endless questions. Many thanks go to my parents who don't understand why this has taken so long to complete. The list of excuses range far and wide, but the important thing is that I actually finished. To all of my friends who have been with me through this, I can't thank you enough. I would've cracked a long time ago if it weren't for the family dinners, candid discussions, cold weather camping trips (that includes field work) and lots and lots of laughter. To all of you I owe so much. If any of you need a field assistant… To all of my field assistants, Tom Lapen, Zach Gustafson, Brian Gouran, Allison Dean and Jeff Laub, thank you for enduring rattlesnakes, wayward boulders and rough waters on Lake Chelan. I couldn't have done this without your help. To Ned Brown, your original idea for a thesis on the Cooper Mountain pluton got run-amuck by geophysics, but to you I'm grateful for getting me started. To Sue DeBari, the busiest woman I know, thanks for spending what little spare time you had with me and for giving me a realistic perspective on thesis writing. Thank you to Liz Schermer for reading a copy back in December and giving me lots of helpful suggestions. To Clark Morgan, thank you so much for listening to complaint after complaint after complaint this past year. It meant so much to have you as part of my support system. Last, but certainly not least, huge thanks go to George Mustoe who was

always there to remind me that there's more to life than the Environmental Studies building. Thank you, thank you, thank you.

I'd also like to acknowledge The Geological Society of America, Sigma Xi Research Society, The Geology Department and the Bureau of Faculty Research, WWU for providing funding for this project.

TABLE OF CONTENTS

LIST OF FIGURES

LIST OF TABLES

TITLE

TECTONIC IMPLICATIONS OF MAGNETIC FABRICS AND REMANENCE IN THE COOPER MOUNTAIN PLUTON, NORTH CASCADE MOUNTAINS, WASHINGTON

INTRODUCTION

Recent structural studies have shown the usefulness of fabric analysis of plutons in elucidating regional tectonics and mechanisms of plutonism. Distinctions have been made between solid-state and magmatic fabrics (e.g. Paterson et al. 1989). Magmatic fabrics can owe their origin to stresses of either pluton emplacement or regional tectonics (see reviews by Bouchez 1997 and Paterson et al. 1998). Tectonically-controlled magmatic fabrics are not only indicators of regional strain, but as these fabrics are developed during pluton crystallization, they therefore can constrain the age of deformation if the pluton is dated (e.g. Benn et al. 2001).

A problem often encountered in fabric study of plutons is weak development of the fabric such that it is difficult to measure and often is visible only in small portions of a pluton. In these instances, measuring magnetic fabric is advantageous because even subtle anisotropy can be easily detected magnetically. The procedure that has been developed for this purpose measures the magnetic susceptibility of minerals in a rock to determine overall rock fabric (anisotropy of magnetic susceptibility – AMS) (e.g. Uyeda et al. 1963, Hrouda 1982). Examples in which this technique has proved successful include the following. The Archean Barnum Lake and Trout Lake plutons near Thunder Bay in the Canadian Shield (Borradaile and Kehlenbeck 1996) preserve a visible

emplacement-related fabric at the margins. Also, a pervasive magnetic fabric was documented, in the absence of visible fabric, which suggested a tectonic origin. The Late Cretaceous Mono Creek granite in the Sierra Nevada of California (Tikoff and de Saint Blanquat 1997) contains macrostructural, microstructural and magnetic fabric all interpreted as syn-magmatic due to shearing of the Rosy Finch Shear Zone. Furthermore, the Prosperous Suite of granites in the Slave Province of the Canadian Shield contains macroscopic foliation as well as magnetic foliation and magnetic lineation that record deformation during transpression (Benn et al. 1998). Fabric analysis, primarily by AMS, of the Eocene Cooper Mountain pluton (Barksdale 1975) is the subject of this report. This fabric analysis was carried out with the expectation that results would either bear on the emplacement mechanism of the batholith or lead to better understanding of the regional tectonic history.

Paleomagnetism was analyzed in the Cooper Mountain pluton, in addition to AMS, for the purpose of evaluating the degree to which the body as a whole has been reoriented since cooling. Some older plutons of the Cascades show significant paleomagnetic discordance with respect to the North American direction of the same age, indicating either tilt or large-scale translation (e.g. the Cretaceous Mt. Stuart batholith, Beck and Nosen 1972). If paleomagnetism indicates reorientation, then the AMS fabrics must be corrected for this in order to be applicable to understanding of regional strain.

GEOLOGIC SETTING

The Cooper Mountain pluton (CMP) is located in Chelan and Okanogan Counties in the North Cascade Mountains of Washington (Figure 1). It is a 48 Ma (K-Ar biotite

age, Tabor et al. 1980) granitic to granodioritic pluton with an aerial extent of 300 km^2 (Barksdale 1975) (see Appendix A for modal comparisons). It was emplaced when the orogeny of the North Cascades Crystalline Core was coming to an end (Haugerud et al. 1994). The Crystalline Core is a block of metamorphic and plutonic units bounded by the Straight Creek Fault on the west and the Ross Lake Fault Zone (RLFZ) on the east (Figure 1c). The orogeny of the Crystalline Core began in the Cretaceous and extended into the Tertiary (Mattinson 1972, Tabor et al. 1980, Haugerud et al. 1994). Some workers suggest a significant component of orogen-parallel dextral transpression (Brown and Talbot 1989) during this orogeny, while others emphasize evidence for SW-directed thrusting (Paterson and Miller 1998). The Crystalline Core itself is divided into two distinct blocks by the NW-striking Entiat fault (Figure 1). The CMP is located in the eastern of these two blocks, the Chelan block, and is the focus of this paper.

By the Early Tertiary, the orogeny had subsided in much of the North Cascades Crystalline Core. There was dextral strike-slip faulting along the Straight Creek Fault (Misch 1966) (Figure 1c). Some workers find evidence for similar displacements on the Ross Lake Fault Zone (Misch 1966, Haugerud et al.1991a). Others interpret the RLFZ as a continuous crustal section between two large-scale folds in the Skagit Gneiss Complex and Jurassic-Cretaceous Methow Basin (Kreins and Wernicke 1990). In the strike-slip scenario, the Ross Lake Fault Zone records dextral movement until ~45 Ma when the Ross Lake Fault Zone is truncated by undeformed, post-tectonic plutons (Haugerud et al. 1991b). These plutons cut-across the Ross Lake Fault Zone and there is no displacement at their margins. The CMP is one of these post-tectonic plutons intruding the southern-most extension of the Ross Lake Fault Zone, the Foggy Dew fault (Figure 1b). On its

western side, the CMP intrudes rocks of the Skagit Gneiss Complex (Haugerud et al. 1991b) and Twenty-five Mile Creek Unit (Figure 1b). Nearly 2-km of vertical relief is exposed in this area along glacially carved Lake Chelan. This study focuses on this western portion of the pluton (Figure 1b).

Previous work includes a study by Wade (1988) who looked at emplacement fabrics of the CMP at its northern margin that includes the truncation of the Foggy Dew fault. He was able to gather few fabric measurements relative to the extent of the field area due to extremely weak flow fabrics. Wade (1988) interpreted foliations parallel to the CMP – Skagit Gneiss Complex boundary to be caused by emplacement of the pluton, but he describes a small area of NW-striking, moderately SW-dipping foliation that does not fit this explanation. He also observed stoping at the margins, which was recognized in our study as well. Wade concluded that stoping was a probable mechanism for emplacement. Raviola (1988) studied the southeastern tip of the CMP but made only one fabric measurement citing weak fabric development. Figure 1b shows the approximate boundaries of the field areas in this, Wade's (1988) and Raviola's (1988) studies.

In a study by Hopson and Mattinson (1999), they concluded that the CMP was fed by melt transported through fractures in the Skagit Gneiss Complex. These fractures formed from extension in the Skagit Gneiss Complex as it was being tilted to the SE (Hopson and Mattinson 1999). Evidence for this tilting comes from contact relations between the Skagit Gneiss and the CMP, a change in dike fabrics from deep to shallow crystallization, and pressure relations indicating an increase in depth from southeast to northwest in the Skagit Gneiss Complex (Hopson and Mattinson 1999).

In this study, the margins of the CMP were observed to be a stockwork of dikes and sills (Figure 2). Blocks of Skagit Gneiss Complex with fabric discordant to the well-defined foliation were found at the CMP – Skagit Gneiss Complex margin. The NW-striking foliation of the Skagit Gneiss Complex is not deflected by emplacement of the CMP. Figure 3 shows fabric orientation in the Skagit Gneiss Complex and the CMP based on field mapping by Wade (1988) and this study. Magmatic fabric is very weak and can be measured in few sites where the foliation is defined by aligned biotite.

PETROGRAPHY

Over 200 oriented hand samples were collected in the field for AMS, paleomagnetic and petrographic analyses. Thirty-five of these samples were slabbed and stained to discriminated plagioclase from potassium-feldspar. Thirteen thin-sections were made of the samples. Thin-section samples were chosen and oriented based on AMS data, in addition to spatial variation throughout the field area.

The CMP is a granite to granodiorite with the following modal composition. The granite contains 30-50% quartz, 29-47% plagioclase, 16-24% potassium feldspar and 2-8% mafic minerals. The granodiorite contains 29-47% quartz, 33-48% plagioclase, 9-26% potassium feldspar and 2-13% mafics. The mafic minerals in both rock types are biotite and hornblende. See Appendix A for QAP diagram, data table and photomicrographs. Figure 4 is a photomicrograph of a granite sample from the CMP. Notice alignment of biotite and lack of solid-state deformation.

Based on modal distribution, the field area could not simply be divided into lithologically characteristic zones. However, there appears to be a textural variability that

can be mapped. Texture in the CMP ranges from fine-grained (≤ 0.3 cm grains) to equigranular, coarse-grained (0.1 to 0.6 cm grains) to porphyritic (0.1 to 0.7 cm quartz and plagioclase) with phenocrysts of potassium-feldspar up to 2.0 cm in size. The porphyritic phase of both modal types is present in NE-SW oriented swaths through the body of the pluton (Figure 5). Note that only 35 sites were included in the petrographic study and more ground-truthing needs to be done to conclusively define these porphyritic swaths.

AMS METHODS AND RESULTS

Oriented hand samples were collected from 113 sites in the field and drilled in the lab. One or two block samples were collected per site, one to five cores (average 2) were drilled per block sample with one to three specimens (average 2) per core. The Kappabridge KLY-3 was used to measure the AMS.

Anisotropy of magnetic susceptibility (AMS) characterizes the variability in magnetic susceptibility with orientation in a mineral. Many studies (Bouillin et al. 1993, Cruden et al. 1999, McNulty et al. 2000) have shown that this variation is coincident with petrofabrics in rocks. For all minerals except magnetite, single crystal AMS is controlled by the mineral's crystallographic axes (Hrouda 1982). Thus, measurements of AMS of a rock provide the overall crystallographic preferred orientation of the minerals in the rock. In many rocks, AMS is controlled by an Fe-rich silicate such as biotite (Hrouda 1982, Borradaile and Henry 1997).

F-statistics were calculated for each specimen to determine whether the magnetic susceptibility is significantly anisotropic (Tauxe 1998). Two specimens were omitted

from further analysis because their F-values were within the 95% confidence level for isotropy. The remaining specimens were analyzed using a bootstrap procedure to determine the scatter (or uncertainty) in the orientation of the AMS axes (Constable and Tauxe 1990). The scatter relates to the shape of the AMS ellipsoid, which indicates preferred crystal orientation within the rock. Three axes of susceptibility define the AMS ellipsoid. An overlap in the degree of scatter between two of the three axes makes mineral orientation distinguishable as prolate or oblate. The maximum, intermediate and minimum axes of susceptibility (k) are denoted throughout the text as k_{max}, k_{int} and k_{min}, respectively. Magnetic foliations were plotted as the k_{max}-k_{int} plane and lineations were plotted as k_{max}. Therefore, for uniaxial oblate sites, only foliation directions were included in the analysis, and for uniaxial prolate sites, only lineation directions were included. In all, foliation data from 14 sites and lineation data from 13 sites were omitted because the uncertainty in orientation of the axes of susceptibility was too high (there was overlap in the scatter for the AMS ellipsoid; the sites appear as dots in Figure 6). See Appendix B for the statistical analysis of the AMS ellipsoid.

Figure 6 shows the magnetic fabric throughout the study area. The area was divided into six different geographic zones with accompanying equal area plots. Poles to foliation plotted in Figure 6a show predominately NW-striking, moderately to steeply dipping foliation. Lineation trends NW-SE with a gentle to moderate plunge (Figure 6b). Figure 6 also shows that in some zones of the pluton, immediately adjacent to the margin, foliation has an east-west strike and a moderate to steep dip (zone E). Zones A and D have a few sites that show this same margin-parallel trend.

The oblateness and prolateness of the AMS shape fabrics were characterized using P- (Nagata 1961) and T-values (Jelinek 1981). P-values ($P = k_{max}/k_{min}$) describe how anisotropic a sample is. The average P-value for the CMP was 1.058 (5.8% anisotropy; P-values ranged from 1.006 to 1.216) which is typical for a pluton with weak flow fabric (Borradaile and Kehlenbeck 1996, Bouillin et al. 1993, McNulty et al. 2000). Figure 7a is a contour map showing that the majority of the field area has < 5% anisotropy with small areas of higher anisotropy. T-values provide a sense of shape for the AMS ellipsoid (T = -1 is truly prolate, T = 1 is truly oblate). Keep in mind that T-values demonstrate whether a specimen is more strongly lineated or more strongly foliated but does not give any indication as to whether the axes of susceptibility are statistically well defined (see Appendix B for a comparison of shape parameters). The average T-value for the CMP was 0.050 (oblate/foliation is more developed), but there was quite a bit of variability within some sites and none of the sites was truly uniaxial oblate or prolate meaning that both foliation and lineation are variably developed which, again, is common in plutons with weak flow fabrics (see previous P-value citations). Figure 7b shows the T-value distribution throughout the study area.

Modal analysis showed that the CMP varies from granite to granodiorite with no logical pattern based on modal distribution (see Appendix A). Bulk susceptibility was compared to modal variation revealing that there was a wide range of distribution in susceptibility data (Figure 7c) and, like model distribution, no discreet pattern could be found. Average bulk susceptibility was 1.045×10^{-4} (for a standard 10 cm^3 specimen). Typically, samples with more mafic minerals display higher magnetic susceptibility. The mafic mineral content in the pluton ranged from 2% to 13% with < 1% of ferromagnetic

minerals (magnetite) contributing to magnetic susceptibility. This yielded enough variation where a simple spatial, lithologic-versus-susceptibility correlation could not be made.

It is important to know which minerals contribute to the AMS of a specimen to know how the fabric orientations should be interpreted. For a few minerals, such as single-domain magnetite, k_{min} corresponds to the *long* axis of the mineral and k_{max} corresponds to the *short* axis resulting in the fabric appearing to be inverse (Potter and Stephenson 1988). Typically, for specimens with a low magnetic susceptibility (less than $5x10^{-4}$), paramagnetic minerals (biotites) control the AMS (Hrouda and Jelinek 1990). However, single-domain magnetite also has low susceptibility and interpretation of the AMS ellipsoid for single-domain grains is different from multi-domain grains or paramagnetic minerals. To identify the dominant AMS carrier for the CMP three different analysis techniques were used. First, the Kappabridge CL-3 was used to measure magnetic susceptibility at low temperature (-192° to 10°C) in order to separate the paramagnetic from ferromagnetic components. Sixteen sites were analyzed to span the range of bulk susceptibility observed. Eleven (69%) sites had a paramagnetic signature, four (25%) had a ferromagnetic signature and 1 (6%) showed equal paramagnetic and ferromagnetic contribution (Figure 8). For those sites with a ferromagnetic susceptibility component, the magnetic fabric was similarly oriented to either magnetic or visible fabric measurements from adjacent sites (see Figure 9). This suggests that the ferromagnetic minerals are oriented parallel to the paramagnetic ones.

Further analysis of the ferromagnetic component showed that both single-domain and multi-domain magnetite grains are present. The magnetic remanence of five

specimens was measured over a temperature range of 20 to 300 K using the MPMS-2 at the University of Minnesota Institute of Rock Magnetism. Figure 10 shows that at temperatures between 20 to 120 K, single-domain magnetite have a higher magnetic remanence when a high magnetic field (2T) is applied as the sample is cooled from room temperature (Dunlop and Özdemir 1997). Both multi-domain magnetite and other non-ferromagnetic minerals do not display this increase in magnetic remanence during cooling in a high magnetic field. All five specimens analyzed contained some single-domain magnetite.

Hysteresis loops were obtained for eight specimens to further classify the size and quantity of magnetite grains. Seven of the hysteresis loops show no indication of ferromagnetic minerals (Figure 11). This suggests that the quantity of magnetite grains is so low that the paramagnetic minerals are overshadowing them. The single specimen with a hysteresis loop proved to be multi-domain magnetite because of the high remanence to saturation ratio. See Appendix B for data. The combined analysis of two types of low-temperature thermomagnetic experiments and hysteresis loops strongly suggests that the paramagnetic minerals are the dominant contributor to magnetic susceptibility.

PALEOMAGNETIC METHODS AND RESULTS

Magnetic minerals within a specimen may preserve a paleomagnetic field direction. By measuring a specimen's remanent magnetization the paleomagnetic field direction can be determined. This can be compared to a reference direction expected for the stable craton. If the observed and reference directions are different, the rock body

may have been reoriented. The paleomagnetism of the CMP was studied to determine if such reorientation had occured. Specimens used for the non-destructive AMS study were measured for magnetic remanence using a 2G-755 cryogenic magnetometer housed in a magnetically shielded room.

Specimens from more than 90 sites were thermally demagnetized in a custom-built magnetically shielded oven, also within the shielded room (see Tables 1 and 2). Remanence in most specimens was unblocked by 370°C, magnetization in all but one of the remaining specimens was unblocked by 600°C. Linear segments of demagnetization paths were visually identified on orthogonal diagrams (Zijderveld 1967) as components of magnetization. Directions of those components and the maximum angular deviation (MAD) were obtained with principal component analysis (Kirschvink 1980). Two remanence components were extracted from the demagnetization data. Orthogonal plots (Figure 12) show the thermal demagnetization paths and the two components. In the following sections, the component demagnetized at lower temperatures is referred to as component 1 whereas the highest temperature component is referred to as component 2.

Several approaches were employed to determine what magnetic minerals carry the remanence. High temperature thermomagnetic experiments established magnetite as a remanence carrier. Figures 13a and 13c are graphs of the experiment showing a drop in susceptibility at ~580°C, which corresponds to the Curie temperature of magnetite suggesting magnetite is the only remanence carrying mineral present. This was apparently confirmed when magnetite was the only opaque mineral identified using reflected light microscopy (see Appendix A) and by an intensity drop below 600°C (Figure 13d), near the Curie temperature of magnetite. However, thermal

demagnetization shows that most specimens lose 90% of their intensity by 370°C instead (Figure 13b). This low unblocking temperature corresponds to the Curie temperature of pyrrhotite. To resolve this discrepancy, the Lowrie method of thermal demagnetization (Lowrie 1990) was then used to document pyrrhotite's presence. Eight specimens were magnetized at 30, 80 and 200 mT along three orthogonal axes (x, y and z, respectively). These particular strengths of magnetizing fields were chosen to match the different coercivity ranges of the expected magnetic minerals and different grain-sizes of ranges (see Appendix C). Figure 14 is a graph of one experiment using the Lowrie method. For all three axes the unblocking temperature was ~340°C which is a pyrrhotite signature. Therefore, both pyrrhotite and magnetite are interpreted as the paleomagnetic remanence carriers for the CMP.

Directions of both components 1 and 2 are scattered, with some upward directions (Figure 15). This suggests that some of the remanence dates from a time of reverse polarity of the magnetic field. Some of the scatter might result from magnetizations recording transitional fields, or mixture of the two polarities. To help reduce the contribution to scatter from demagnetization paths that result from simultaneous demagnetization of opposite polarity magnetizations, only line segments with MAD < 8 degrees were used. Futhermore, to reduce bias that might arise from inproperly separating the polarities to calculate their mean directions, the bootdi method of Tauxe (1998) was used. This first employs a PCA approach to divide the dataset, then evaluates whether either set has a Fisherian distribution (Fisher 1953), and, if so, calculates the mean and Fisher statistics.

The mean direction of component 1 is D = 343.5, I = 73.2, α_{95} = 6.7 and k = 12. The mean direction of component 2 is D = 342.7, I = 72.8, α_{95} = 9.2 and k = 17. The upward directions were not included in this analysis because they are too poorly constrained (scatter is too large). The present day field direction in the field area is D = 20.9, I = 71.7 and the expected North American Eocene direction is D = 349.5, I = 67.4 (Diehl et al. 1983). See Tables 1 and 2 for a list of site data and Figure 16 for a plot of component 1 and component 2 data.

Component 1 and 2 mean directions were calculated assuming a Fisher distribution of data (a circular distribution about the mean). Component 2 is Fisher distributed while component 1 is slightly elongate. There is an underlying E-W elongation in the data set that makes use of Fisher statistics inappropriate although not necessarily inaccurate. However, one can see from Figures 15 and 16 that the two components of magnetization are very similar suggesting that both magnetite and pyrrhotite record the same direction, not much different from the expected Eocene direction.

Noting the grain-size variation in the CMP and the NE-SW swaths of porphyritic phase rock (see Figure 5), the paleomagnetic data were reevaluated to determine if the porphyritic phase records a different direction than the other petrographic phases. The results, nonetheless, confirmed that all the phases record, on average, the same magnetic field.

As far as the underlying E-W elongation of directions goes, more analysis needs to be done to isolate this elongation and determine the significance, if any. Beck (1999) has discussed the significance of shape analysis and various ways in which to approach it.

If this elongation does prove to be significant, the elongation of remanence of the CMP could be resulting from a transition in polarity.

DISCUSSION

In a few localized zones within the CMP, AMS fabric parallels the pluton – country rock margin (Figure 6). This fabric is interpreted as an expansion fabric acquired during emplacement because of its concordance with the margin. Wade (1988) proposed emplacement mechanisms for this pluton that include stoping and shouldering aside. This conclusion was based on contact relations and field mapping. The magnetic fabric elsewhere in the pluton (beyond the margins) is interpreted to be expressive of regional deformation rather than emplacement due to the overall NW-SE trend of fabrics in the pluton and discordance of these fabrics with the pluton boundary. Figure 17 shows two lower-hemisphere projections of the predominant trend of these tectonic fabrics. The magnetic fabrics shown in Figures 6 and 17 are interpreted as tectonic alignment of biotite when the pluton was crystallizing. This conclusion for the timing of fabric development is drawn from the lack of solid-state deformation in the rocks (see Figure 4). Therefore, the sub-horizontal lineations in the CMP may suggest two things. First, pervasive fabrics in the CMP show that it is not an undeformed post-tectonic pluton, rather it is a syn-tectonic pluton. Second, the orientation of these fabrics gives some indication of Eocene-age strain in the area, as the fabrics were formed in response to regional strain.

A recent study was done on an older pluton in the North Cascades with similar results to this study. The Late Cretaceous Mt. Stuart batholith has AMS fabrics with a

NW-SE lineation that may record strain during the final stages of crystallization (Benn et al. 2001). These data were then used to investigate two models of plate tectonic history during the Cretaceous, 1) plate convergence orthogonal to the continental margin and 2) plate convergence oblique to the continental margin. Both models are viable to the Eocene Cooper Mountain pluton study however, the later model is more likely and is explained in the following paragraphs.

One model to explain fabric orientation in the CMP involves shear, perhaps associated with the NW-SE faults in the region (i.e. the Ross Lake Fault Zone, RLFZ). The RLFZ is an Early Tertiary fault, thought to be active until ~45 Ma, exhibiting dextral strike-slip motion (Misch 1966, Haugerud et al. 1991b). The younger age limit of fault movement was inferred from evidence that the Golden Horn batholith (GHB) and the CMP were undeformed, post-tectonic plutons that cut the fault trace and fabrics related to it (Haugerud et al. 1991b), however it has been established that the CMP is not post-tectonic. Moderate shear-strain combined with a low angle of plate convergence ($<20^{o}$) will result in horizontal lineations (Tikoff and Greene 1997) much like the magnetic lineations observed in the CMP that are oblique to the regional faults and trend of the orogen. Figure 18a is a model of such a system with the lineation direction horizontal and oblique to the trend of the orogen. Figure 18b shows the obliquity of the lineations.

A second model is orogen-parallel extension (Figure 18c). Some workers studying rocks in the North Cascades Crystalline Core have concluded that there was significant orogen-parallel (NW-SE) stretching during the Eocene (Ewing 1980, Miller et al. 2000). The orogen-parallel extension models assume that shortening was more or less orthogonal to the NW-SE trend of the orogen, producing a sub-horizontal stretching of

the orogeny via pure shear. If this strain regime was active during emplacement and cooling of the CMP, the lineation recorded by AMS should also parallel the extension direction. The obliquity (~30°) between the lineation direction in the CMP and both the major trend of the Cascade orogeny and nearby faults, such as the RLFZ, leads to the favoring of dextral shear strain as the origin of these fabrics.

CONCLUSIONS

On the basis of field mapping alone, the CMP has very little observable fabric. However, AMS was able to discern the subtle anisotropy present. Margin-parallel fabric suggests expansion during emplacement, but AMS reveals an internal, predominant NW-SE trend of foliations with sub-horizontal lineations. These fabrics are consistent with a model of Eocene dextral shearing resulting from regional strain in the North Cascades Crystalline Core. In addition, the paleomagnetic evidence suggests that there was no or little reorientation of the CMP since it cooled below 550°C and therefore, no need to correct the found fabrics for reorientation.

AMS and paleomagnetic work on other plutons in the North Cascades, such as the Eocene Golden Horn batholith, can provide additional data to constrain internal deformation of the North Cascades particularly during Eocene events in the Chelan block of the North Cascades Crystalline Core.

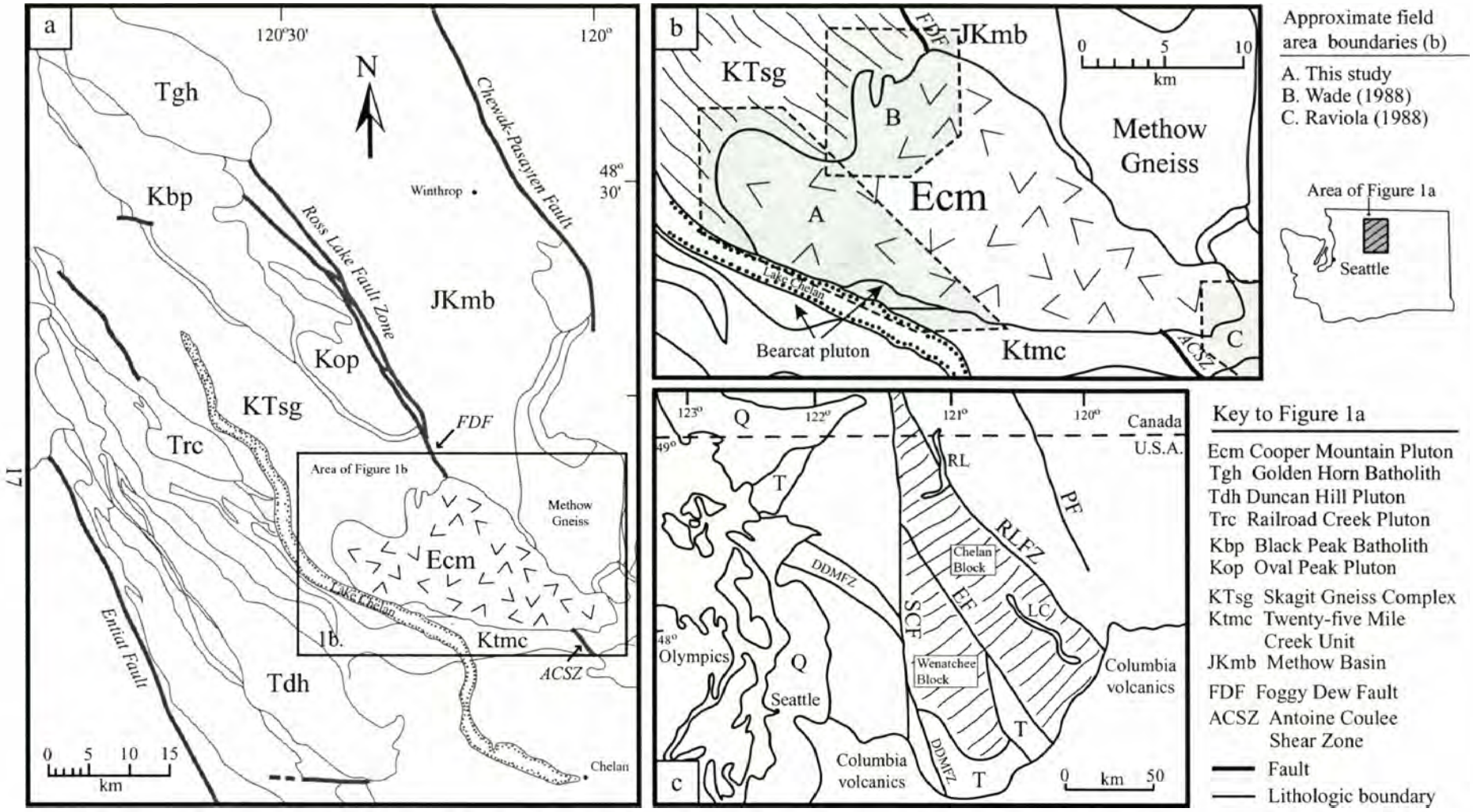

Figure 1. Regional geologic map of the eastern half of the North Cascades Crystalline Core modified from Hopson and Mattinson (1994) (Figures a & b). The Cooper Mountain pluton (Ecm) is indicated by the hash-marks. b) Approximate field areas for this and other studies in the shaded regions. Figures 5, 6 and 7 are the shaded area marked "A". c) Geologic map of northwestern Washington emphasizing the regional faults (modified from Haugerud et al. 1994). SCF = Straight Creek fault, EF = Entiat fault, RLFZ = Ross Lake Fault Zone, PF = Pasayten fault, DDMFZ = Darrington-Devils Mtn. Fault Zone, T = Tertiary sedimentary units and volcanics, Q = Quarternary sediments, RL = Ross Lake, LC = Lake Chelan.

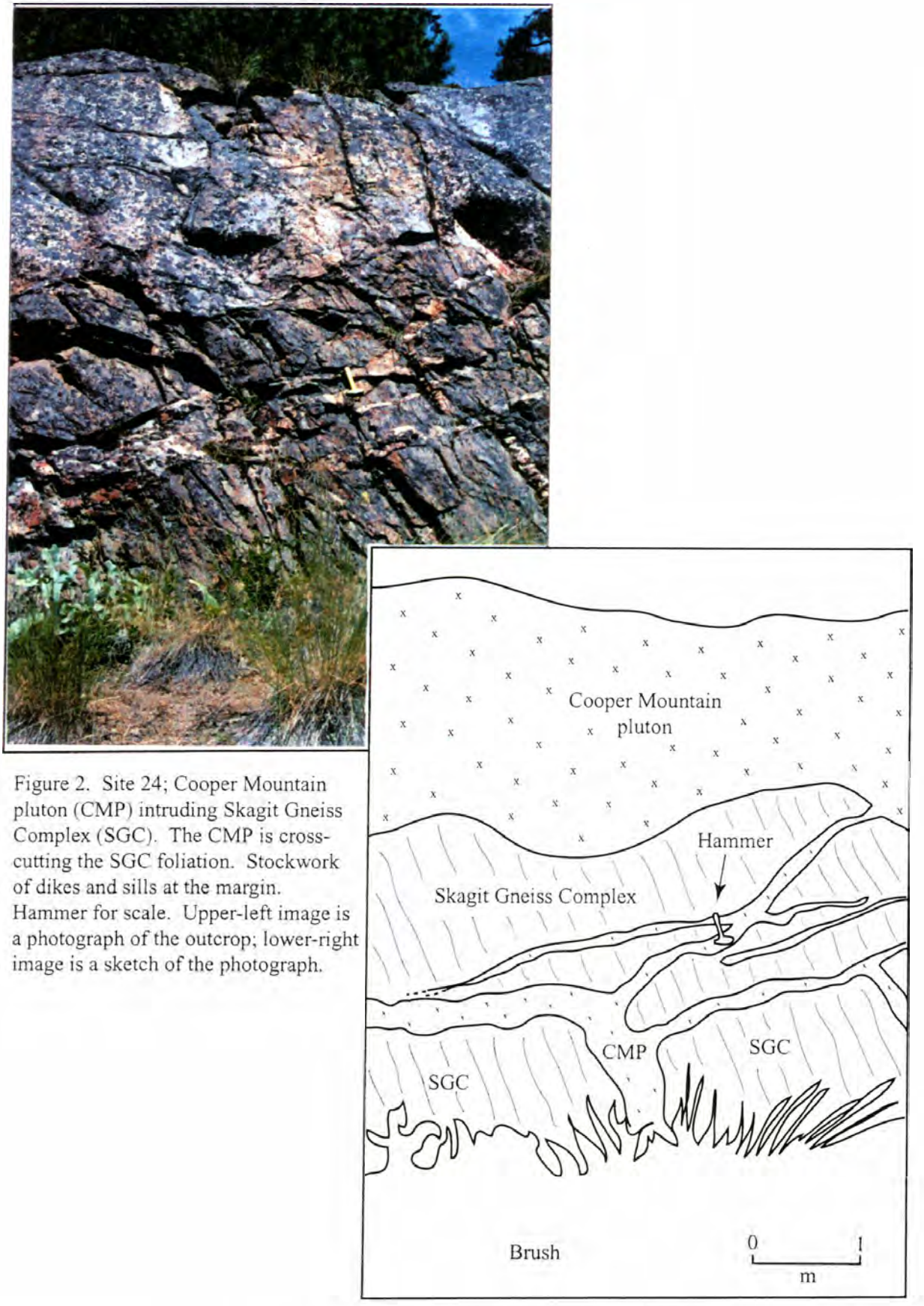

Figure 2. Site 24; Cooper Mountain pluton (CMP) intruding Skagit Gneiss Complex (SGC). The CMP is cross-cutting the SGC foliation. Stockwork of dikes and sills at the margin. Hammer for scale. Upper-left image is a photograph of the outcrop; lower-right image is a sketch of the photograph.

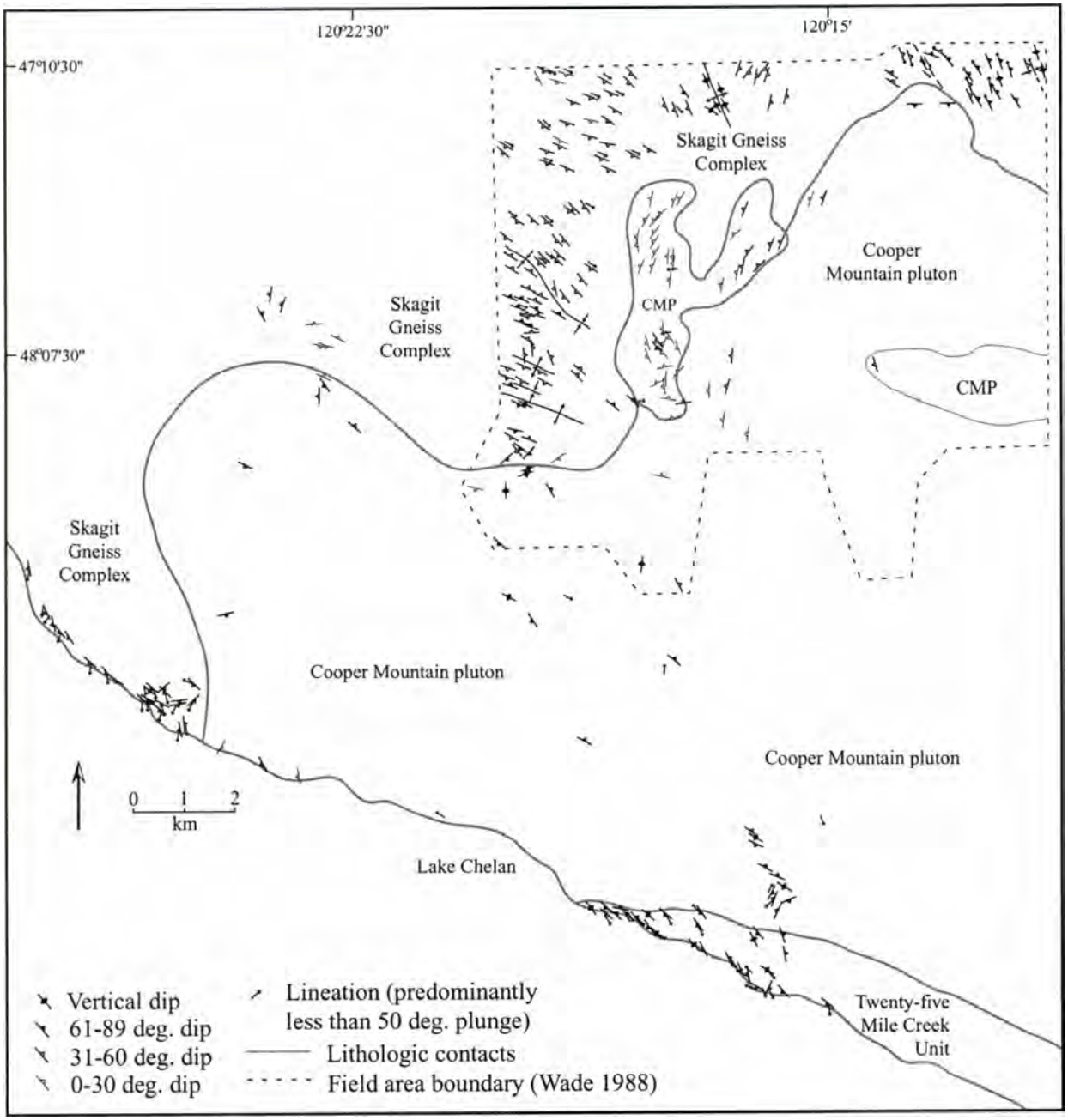

Figure 3. Cumulative fabric maps of Wade (1988) and this study. These are fabrics measured in the field and/or oriented hand sample. Note that very few fabric measurements were taken in the pluton boundary. Wade's field area is outlined with a dashed line, other fabrics measurements beyond the dashed line are from this study. CMP = differently mapped lithologies of the Cooper Mountain pluton (Wade 1988).

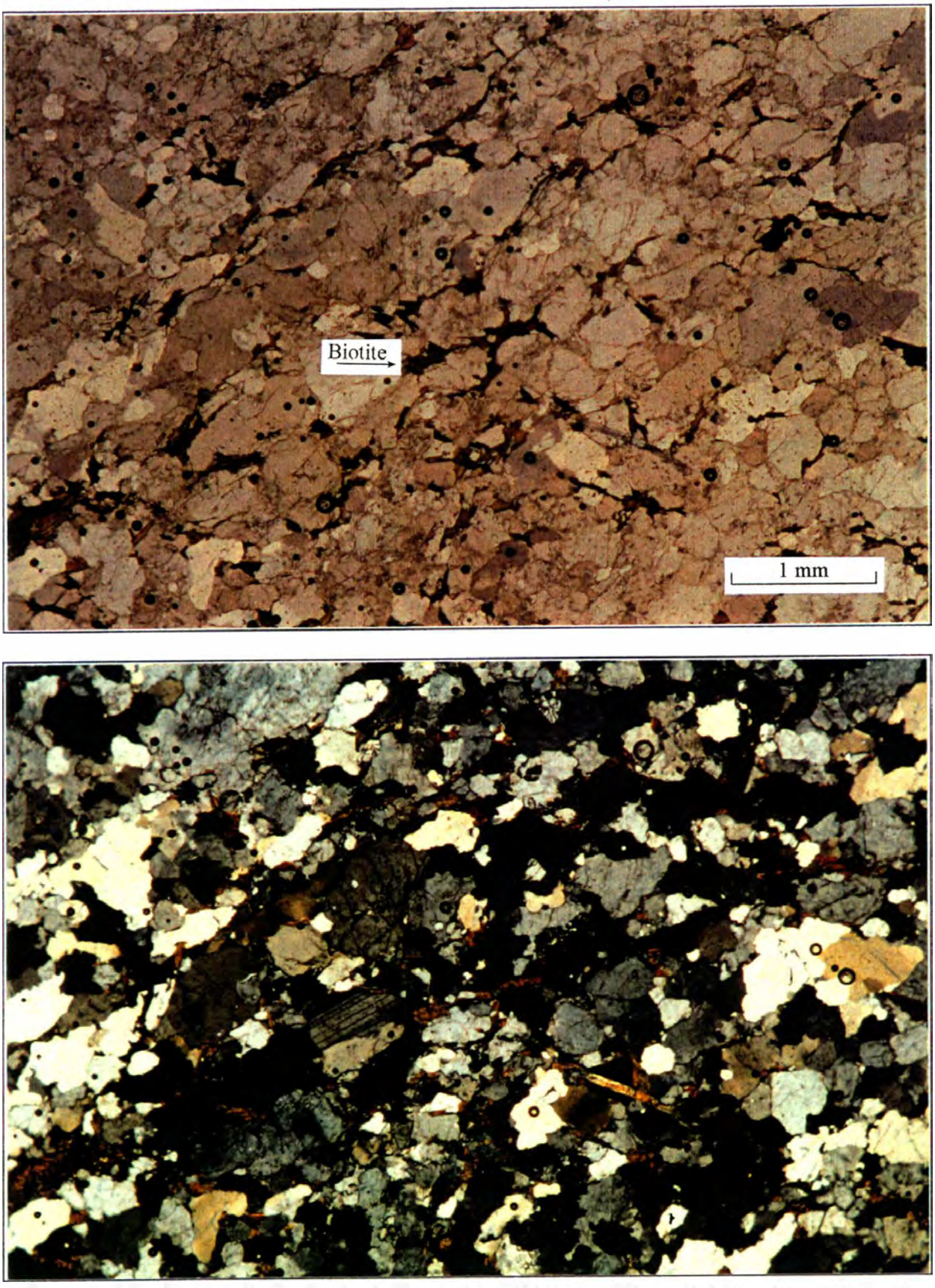

Figure 4. Sample 183-209b, fine-grained granite. Aligned biotites, lack of solid-state deformation. k = 6.29×10^{-5}, P = 1.212, T = 0.344. Upper image in plane-polarized light, lower image in cross-polarized light. Scale = 16x magnification; 4.2 x 6.4 mm.

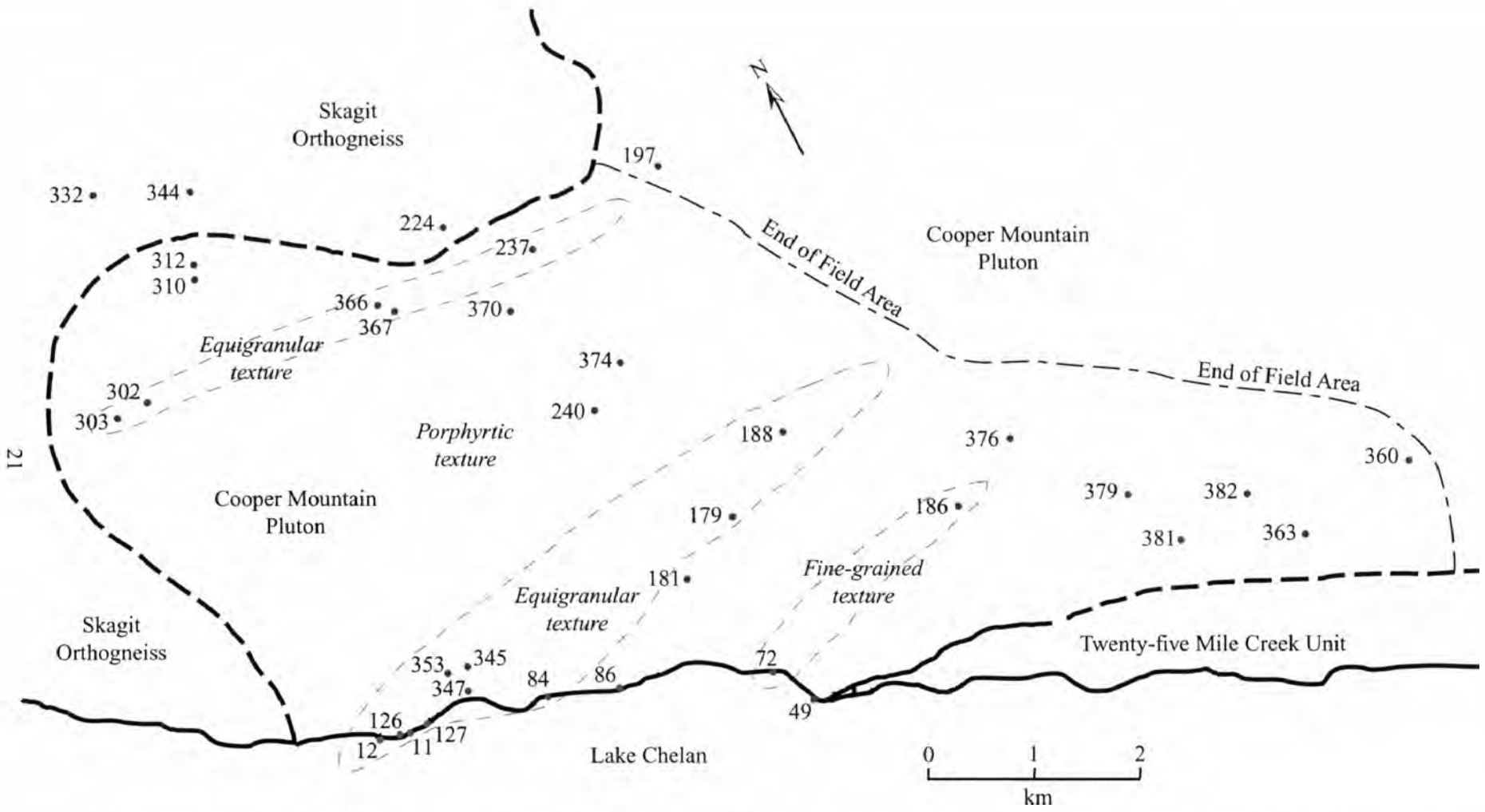

Figure 5. Partial site location map of the Cooper Mountain pluton field area. Sites correspond with petrographic samples in Table A.1. The eastern-most boundary of the field area is shown as a thin, broken-dashed line. Contour lines are drawn and shaded according to textural variation. Two contoured zones are labeled equigranular and one contoured zone is labeled fine-grained. The areas of the pluton outside of those contoured zones is porphyritic in texture.

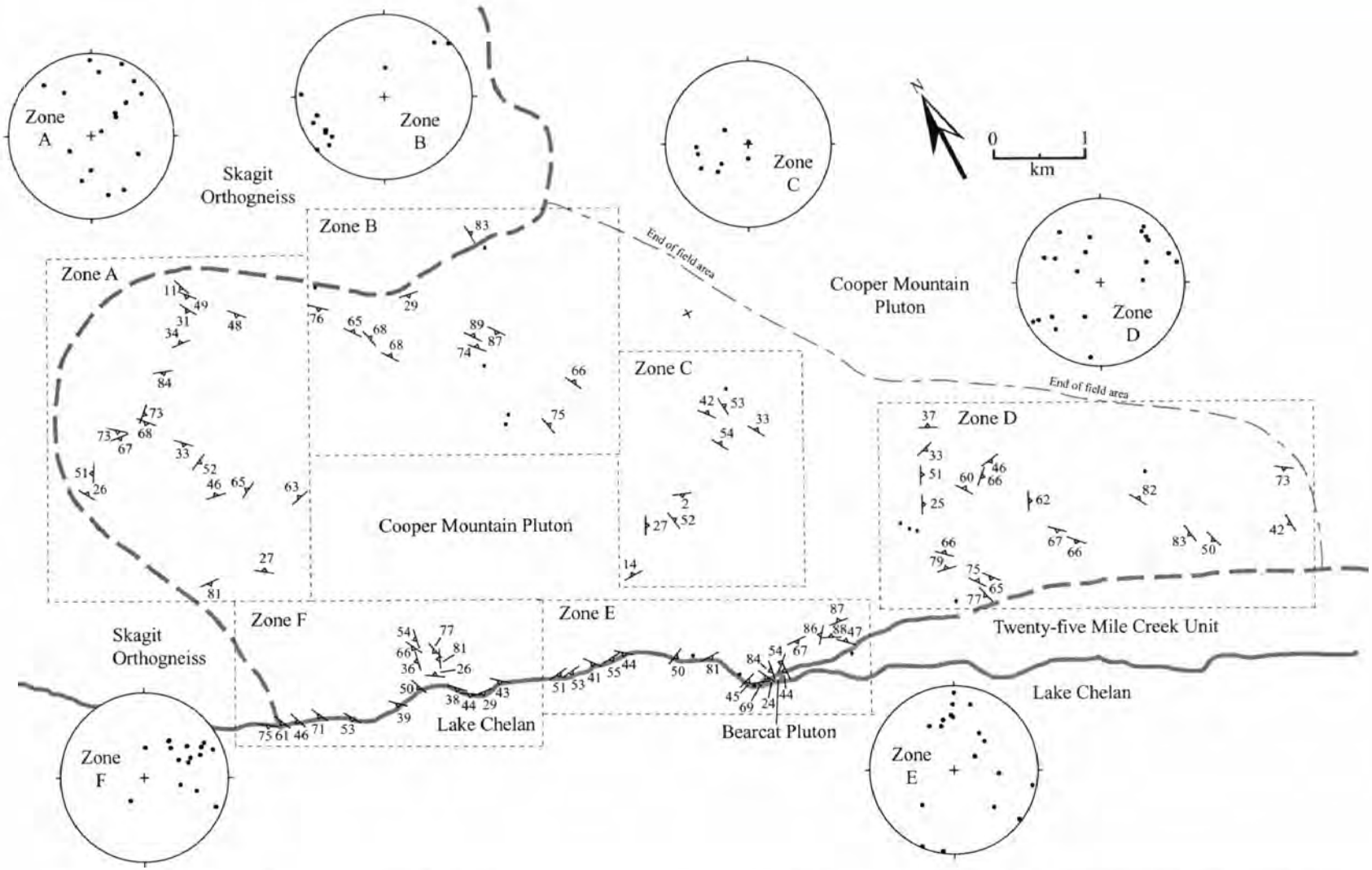

Figure 6a. Magnetic fabric in the CMP. The field area is broken into six zones based on geography, with accompanying equal area plots. a) k_{min} directions (poles to magnetic foliation) plotted. Dots within field area are sites in which foliation or lineation could not be determined with significance.

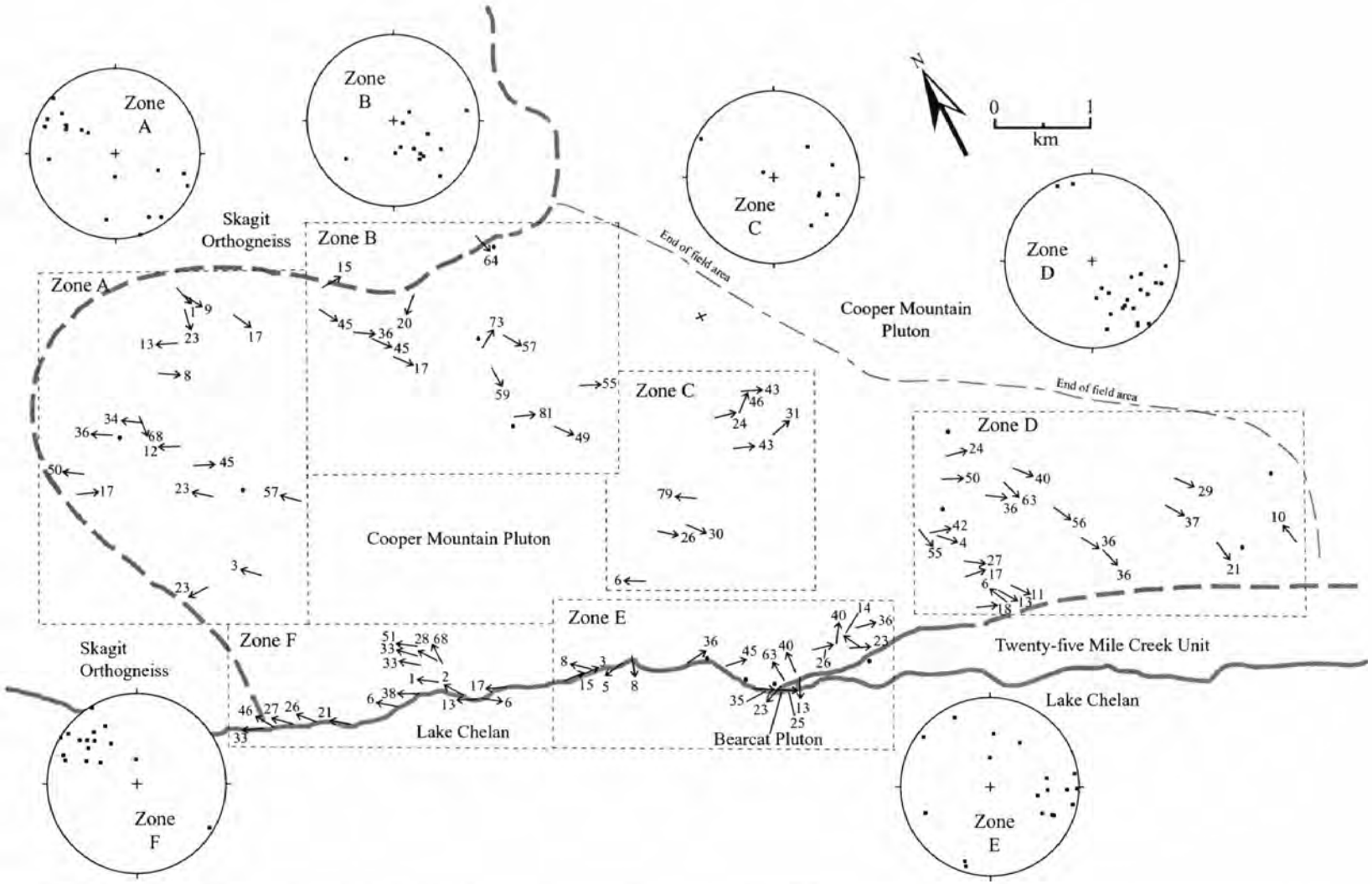

Figure 6b. Magnetic fabric in the CMP. The field area is broken into six zones based on geography, with accompanying equal area plots. b) k_{max} directions (magnetic lineation) plotted. Dots within field area are sites in which foliation or lineation could not be determined with significance.

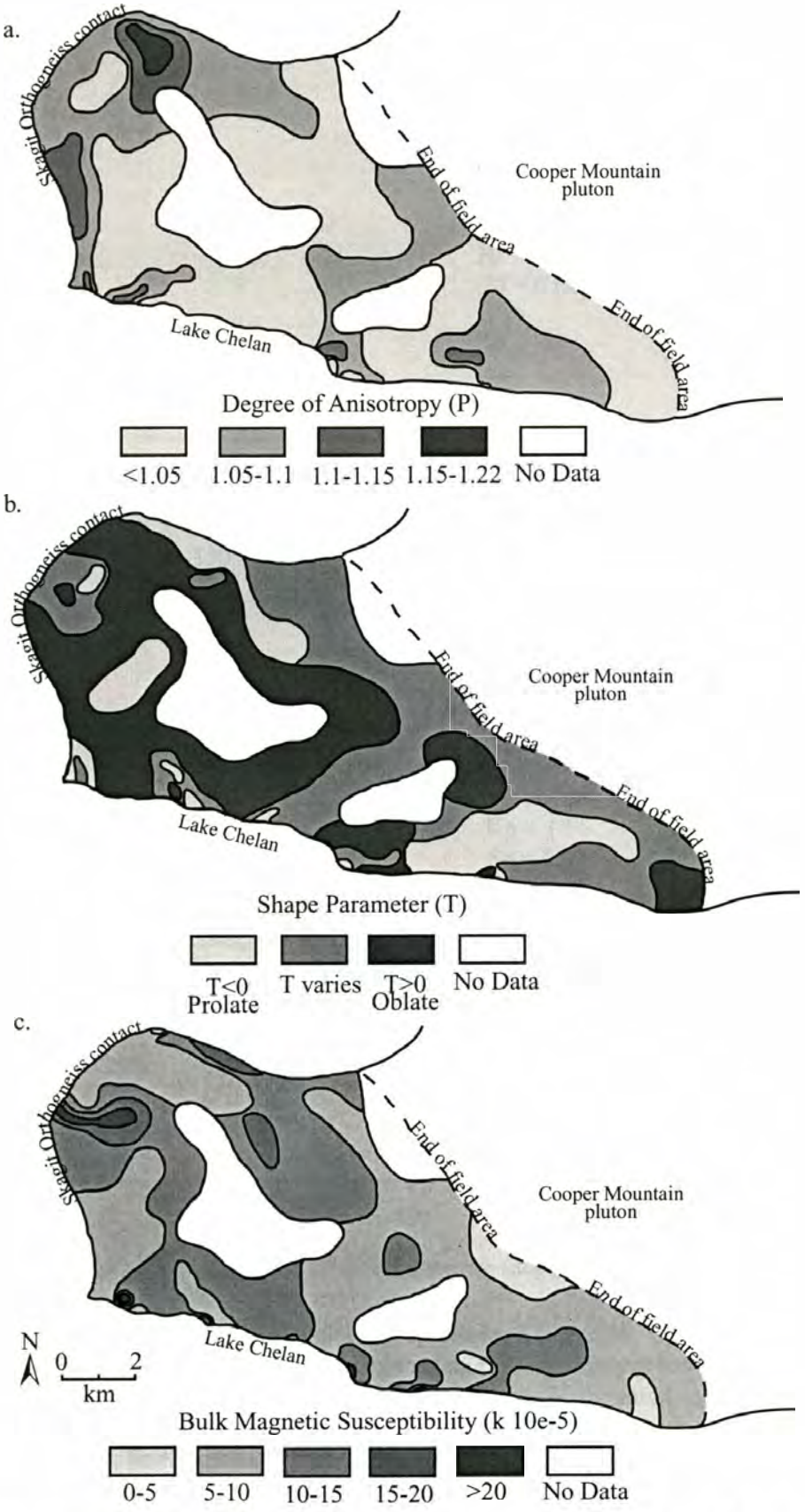

Figure 7. Contoured maps of the field area showing spatial distribution for values of a) anisotropy (P), b) shape (T) and c) bulk susceptibility (k). See Figure 1 for field area boundaries.

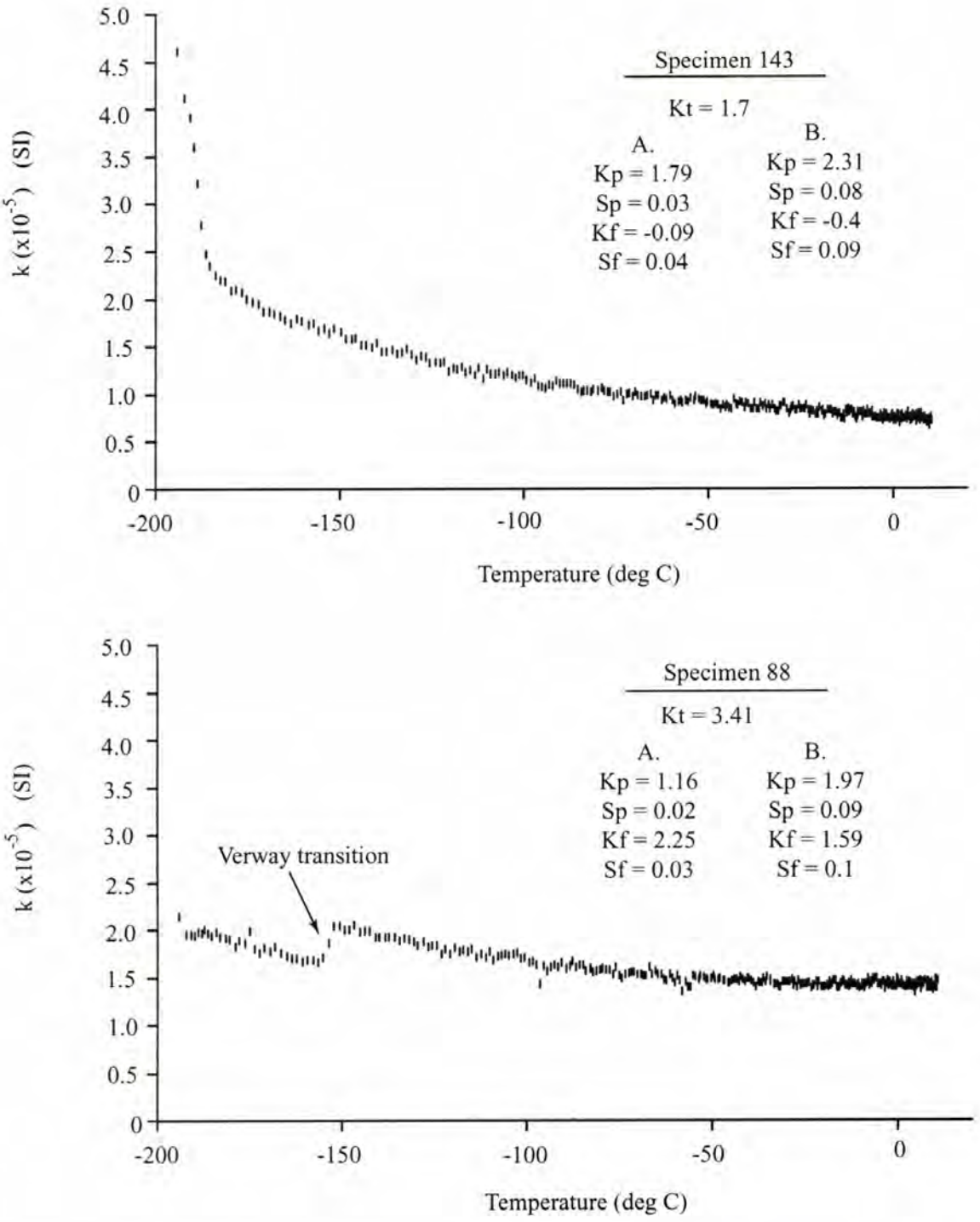

Figure 8. Low temperature thermomagnetic plots for specimens 143 and 88. Specimen 143 displays a dominant paramagnetic component characterized by the large susceptibility at lower temperatures. Specimen 88 displays a dominant ferromagnetic component shown by the small change in susceptibility with temperature and the Verway transition at ~ -150 degrees C. Kt = whole rock susceptibility, Kp = paramagnetic component, Sp = paramagnetic determination error, Kf = ferromagnetic component, Sf = ferromagnetic determination error, A = using the constant ferromagnetic susceptibility method (Hrouda 1994), B = using the sloped ferromagnetic susceptibility method (Hrouda et al. 1997).

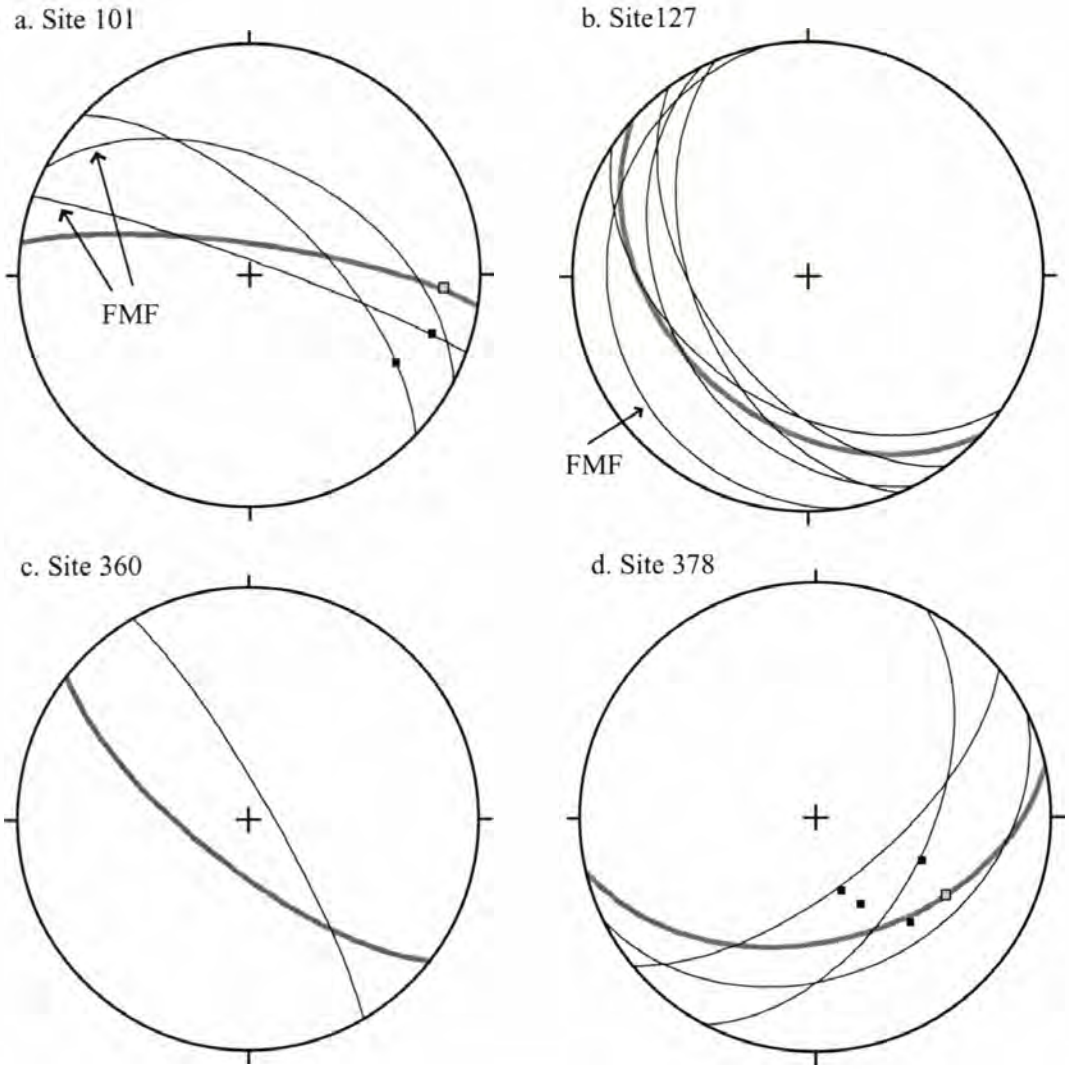

Figure 9. Lower hemisphere projections for the four specimens that displayed ferromagnetically controlled susceptibility with low temperature thermomagnetic experiments. The AMS data for each specimen (thick, gray lines for foliation, open squares for lineation) is plotted against magnetic fabric from adjacent AMS sites and fabric measured in the field (thin, black lines for foliation, solid squares for lineation). FMF = field measured foliation, others are AMS fabrics. The ferromagnetically controlled AMS is oriented similarly to the non-ferromagnetically controlled fabric indicating single-domain inverse fabrics are not present.

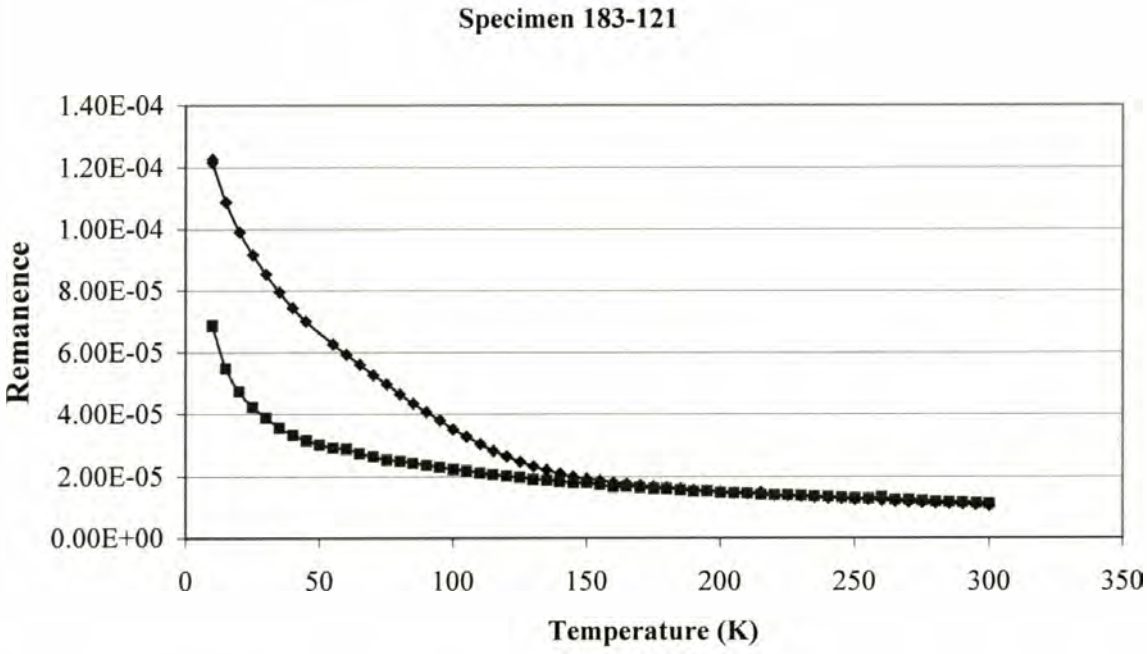

Figure 10. Low temperature magnetic remanence plot from 20 to 300 Kelvin. The lower curve is the susceptibility of the specimen measured in a zero-field environment and the upper curve is the same specimen measured in a 2.5 T field. See text for discussion.

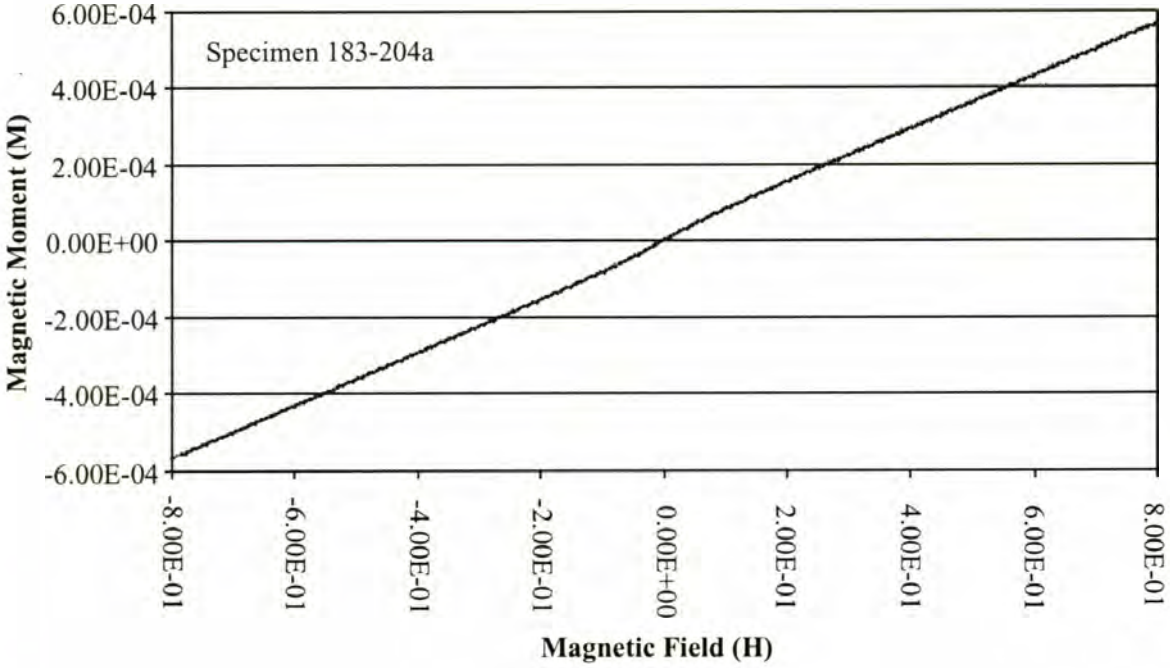

Figure 11. Magnetization of specimen 183-204a in a high-magnetic field. This specimen lacks a hysteresis loop and shows only the high-field slope.

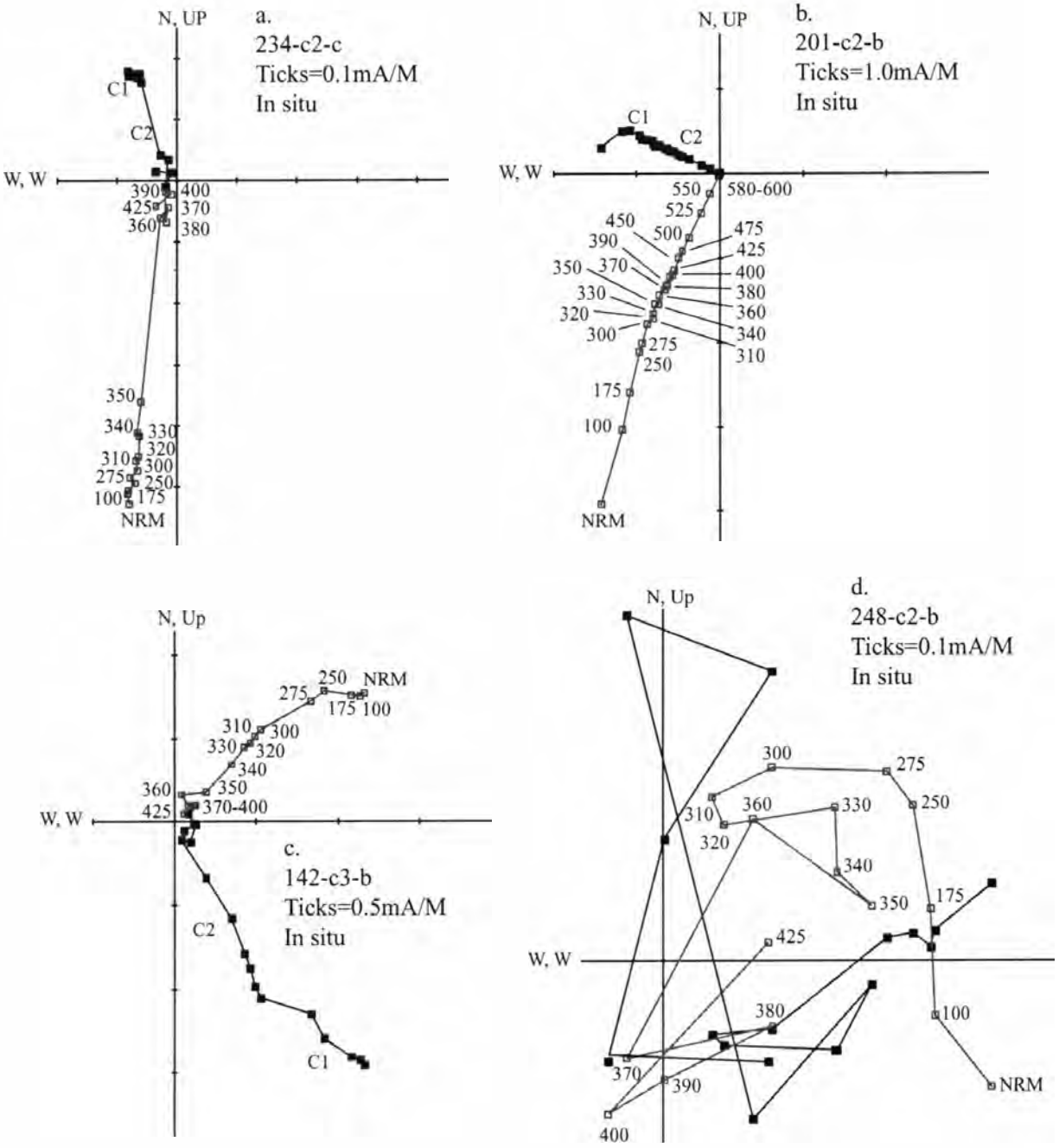

Figure 12. Orthogonal plots for four paleomagnetic specimens. a), b) and c) all contain two components (C1 and C2) with thermal demagnetization steps labeled (degrees C). d) is an example of a specimen with unstable remanence that was subsequently omitted from the data set. Horizontal projection is labeled C1 and C2. Vertical projection is labeled with thermal steps.

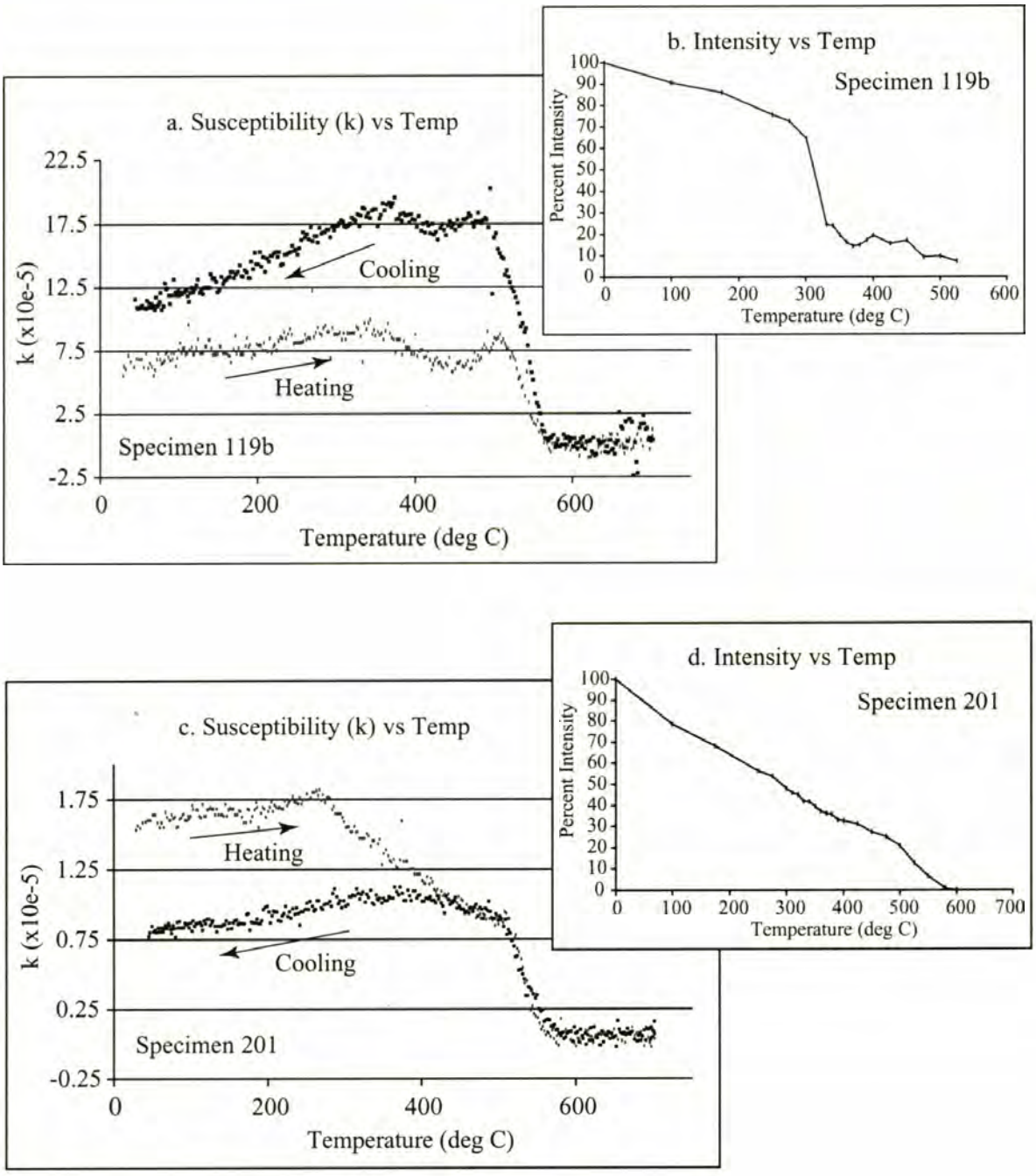

Figure 13. High temperature thermomagnetic plots (a & c) ahowing a dramatic drop in magnetic intensity at ~580 degrees C, which corresponds to magnetite's Curie temperature. Accompnnying demagnetization-intensity plots show that for the same specimens there are two different unblocking temperatures (320 and 580 degrees C).

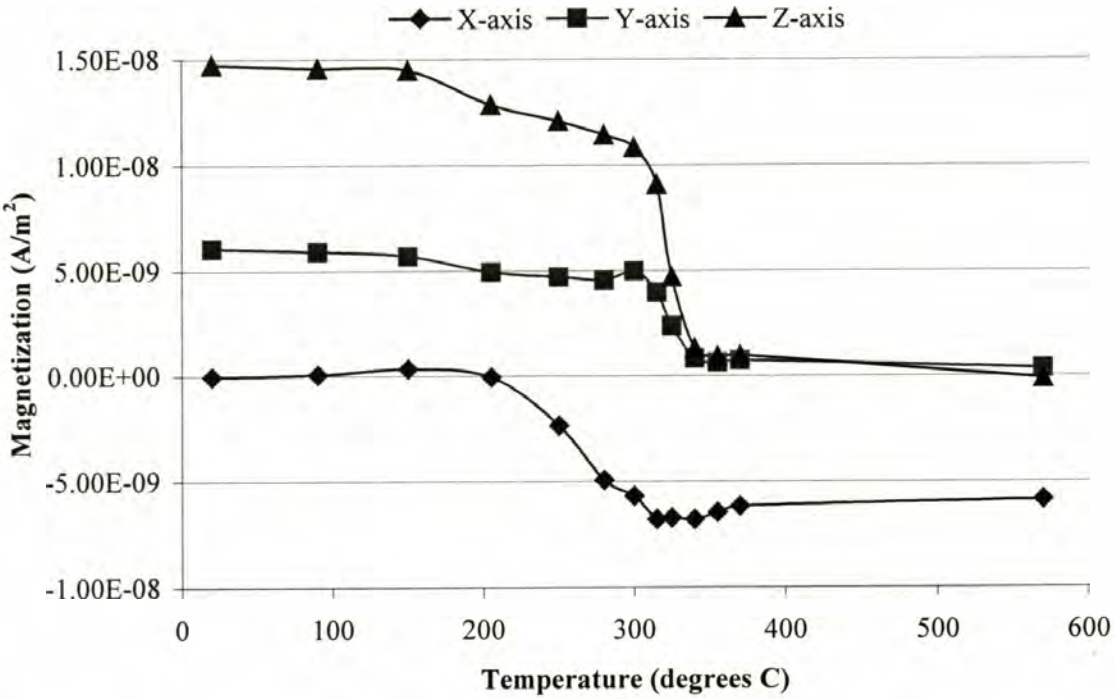

Figure 14. Specimen 66-c1-b thermally demagnetized using the Lowrie method (Lowrie 1990). Notice the drop in intensity between 320°C and 340°C for all axes. See text for discussion.

Specimen	Dec	Inc	Npoints	MAD	Begin T	End T	Angle
114-c1-c	340.0	68.9	5	4.3	310	350	0.3
116-c2-a	24.2	70.0	7	0.6	260	350	0.0
120-c2-a	311.3	70.7	6	6.5	260	340	8.6
121-c1-b	354.6	79.7	5	2.5	300	340	0.3
133a-c1-b	252.2	82.4	4	7.1	100	300	27.9
135a-c1-b	54.8	51.0	4	0.5	225	370	0.1
137a-c1-c	9.7	80.5	8	1.6	210	350	2.4
139-c2-b	4.0	76.2	6	1.6	275	340	0.1
142-c3-b	159.7	-21.8	5	2.0	300	340	7.8
160-c2-a	311.6	53.4	6	7.6	290	350	7.9
200-c1-c	318.6	71.5	8	6.5	150	340	12.9
201-c1-a	23.0	53.7	4	1.9	150	370	0.3
205-c1-b	316.7	72.9	6	7.5	290	350	8.8
211-c1-c	129.9	-29.6	9	2.3	150	350	0.4
213-c1-a	130.1	-3.6	5	6.3	150	370	0.9
214-c2-b	281.5	32.9	4	6.8	250	400	1.4
217-c2-c	60.4	50.5	7	7.3	260	350	0.6
220-c1-b	100.1	26.9	4	7.4	225	370	3.8
229-c1-a	53.6	63.5	7	5.1	250	340	1.1
234-c2-c	344.7	68.5	4	1.1	330	360	4.4
235-c2-c	203.9	-0.9	5	5.8	250	325	135.3
239-c2-b	256.5	52.4	5	2.6	150	370	1.3
247-c1-b	322.5	58.3	4	5.3	250	400	24.6
248-c2-b	86.7	80.4	4	5.1	100	275	98.8
249-c2-a	323.4	75.4	4	2.8	150	370	0.5
251-c1-b	308.0	68.3	4	6.6	320	450	1.2
252-c1-b	222.7	81.5	4	7.9	150	290	22.6
253-c3-b	18.5	74.4	4	2.5	150	370	0.5
254-c2-b	235.0	70.9	6	5.0	290	450	1.1
256-c1-d	45.5	-14.5	4	7.7	330	360	62.1
259-c2-b	335.8	55.9	5	5.2	290	340	2.5
25-c2-b	313.8	52.3	5	7.1	150	370	2.4
261-c1-b	325.8	72.3	9	3.7	150	350	2.9
262-c1-c	321.3	50.6	4	2.4	150	370	0.6
263-c2-a	305.1	35.9	4	2.6	150	370	9.5
28-c1-a	64.0	83.6	9	3.4	90	340	0.2
2-c2-a	335.8	71.8	7	4.7	150	330	0.6
32-c1-b	336.7	56.5	4	6.2	320	350	1.3
35-c1-b	329.0	50.5	5	6.0	290	340	7.6
36-c2-c	339.4	66.8	8	1.9	150	340	0.2
37-c2-b	165.8	-62.9	6	4.6	150	320	179.9
3-c1-d	86.7	76.7	7	5.1	250	340	1.3

Specimen	Dec	Inc	Npoints	MAD	Begin T	End T	Angle
46-c1-b	5.9	66.2	4	5.1	325	370	5.6
65-c1-c	343.4	72.4	7	0.8	250	355	0.0
68-c1-b	358.9	44.0	6	6.5	260	340	1.7
76-c1-c	17.0	80.9	5	5.3	150	370	11.8
82a-c3-b	107.5	-67.0	4	6.2	210	310	33.2
83-c2-c	35.3	66.4	4	4.8	290	330	54.2
84-c1-d	21.8	82.8	5	3.5	150	370	0.5

Table 1. Paleomagnetic directions for pyrrhotite specimens. *Npoints* = number of points in the line or plane fit analysis; *MAD* = mean angular deviation; *Begin T* and *End T* = beginning and ending thermal demagnetization temperature (°C) in the line or plane fit ; *Angle* = angle to the origin.

Specimen	Dec	Inc	Npoints	MAD	Begin T	End T	Angle
004-c1-d	269.2	57.5	7	7.7	390	525	70.9
026-c2-b	343.7	62.7	10	2.9	300	565	0.6
028-c2-b	38.3	71.3	12	4.9	370	600	0.5
065-c2-a	351.0	71.1	9	6.9	370	575	1.1
069-c2-a	36.1	59.9	12	1.4	370	600	0.1
076-c1-c	336.7	66.0	10	7.1	370	585	0.7
123-c2-c	318.8	75.4	14	2.6	340	580	0.2
124-c2-b	310.7	51.2	10	5.9	400	580	1.2
133a-c2-a	290.4	50.8	15	6.6	300	565	10.6
139-c1-b	58.4	76.8	6	5.5	400	565	0.9
201-c2-b	24.4	61.9	18	0.6	300	580	0.0
205-c3-b	39.6	75.5	5	1.7	510	575	0.3
205-c3-b	222.6	-74.0	4	4.0	400	510	177.1
208-c2-a	43.1	69.4	10	1.5	150	535	0.6
236-c1-b	42.7	72.3	17	5.3	100	600	1.8
241-c3-b	178.7	-28.7	4	7.8	620	665	26.8
251-c1-b	308.0	68.3	4	6.6	320	450	1.2
260-c2-b	298.4	61.4	8	5.0	370	565	1.3

Table 2. Paleomagnetic directions for magnetite specimens. *Npoints* = number of points in the line or plane fit analysis; *MAD* = mean angular deviation; *Begin T* and *End T* = beginning and ending thermal demagnetization temperature (°C) in the line or plane fit ; *Angle* = angle to the origin.

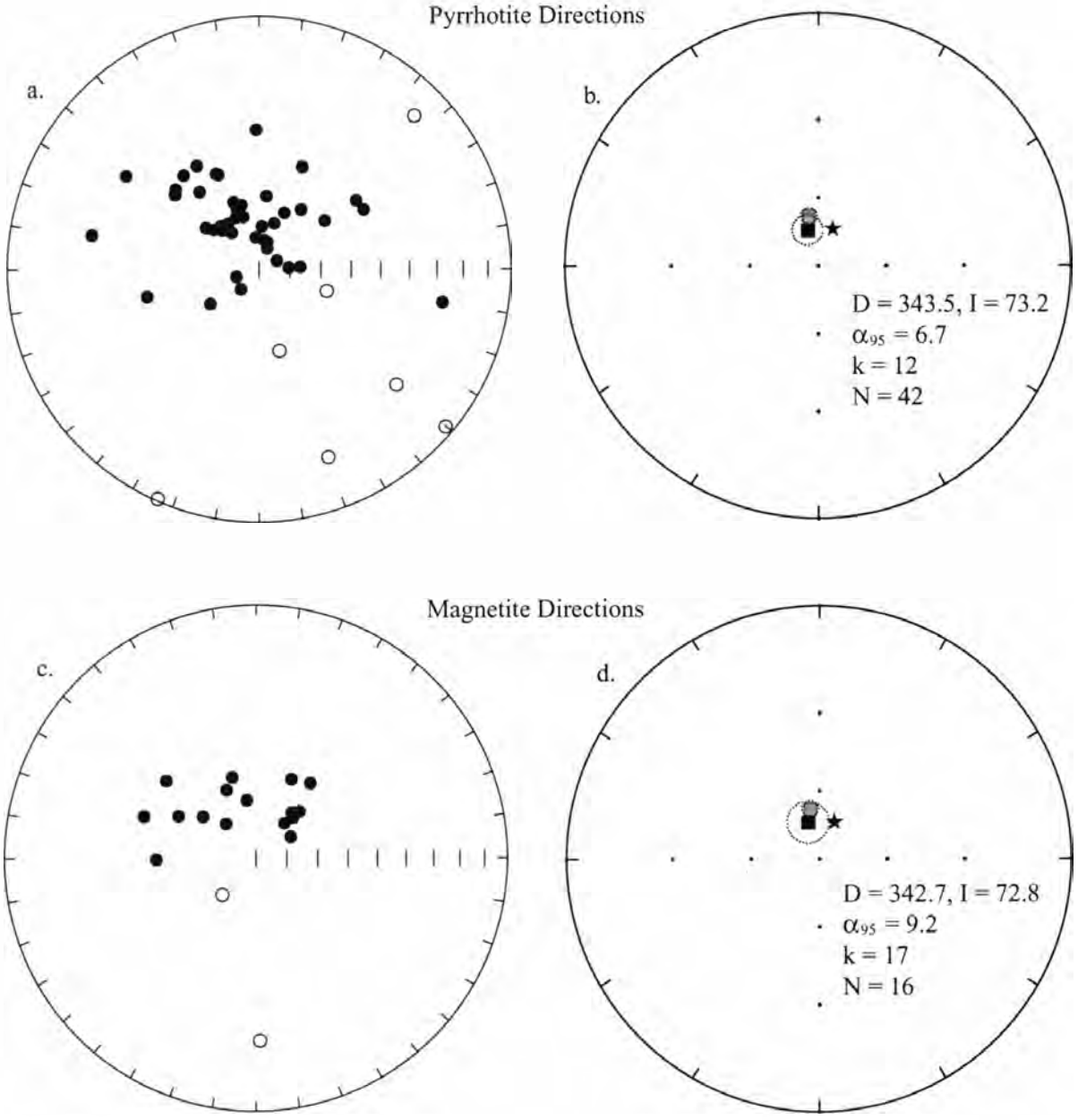

Figure 15. Paleomagnetic directions of both specimens containing pyrrhotite and magnetite as remanence carriers. a) and c) are equal-area projections of individual specimens with either line or plane fits. Closed circles are downward directions, opened circles are upward directions. b) and d) are equal-area projections of pyrrhotite and magnetite mean directions (black squares), the North American Expected Eocene direction (gray squares; Diehl et al. 1983) and the present day field direction (stars). Data listed are the mean declination, inclination, α_{95} , k and N (number of specimens). These data do not include upward directios for they were too poorly constrained.

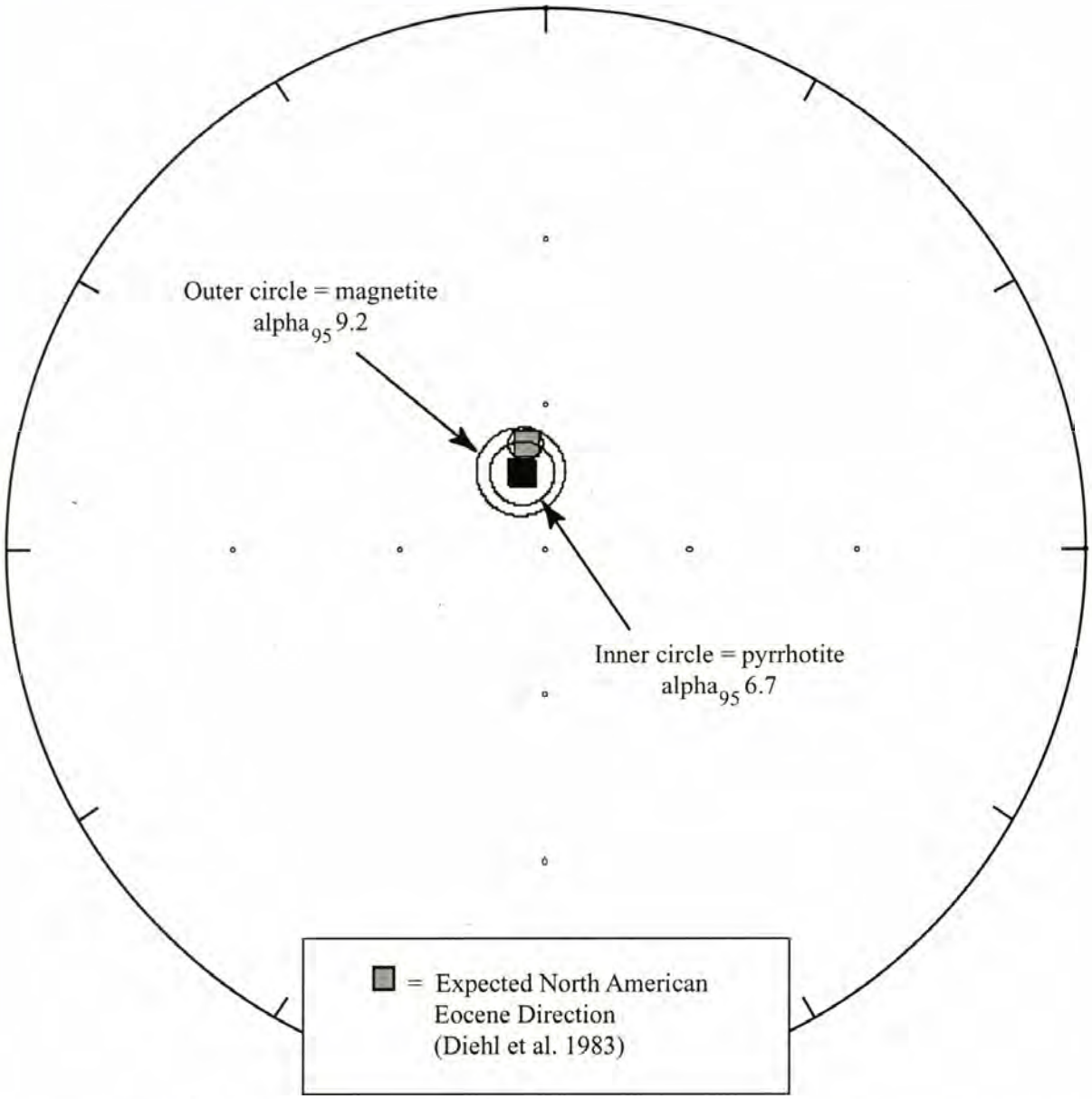

Figure 16. Pyrrhotite and magnetite mean directions plotted against each other with their α_{95} circles of confidence. Pyrrhotite has the smaller α_{95} of 6.7 and magnetite is the larger (9.2).

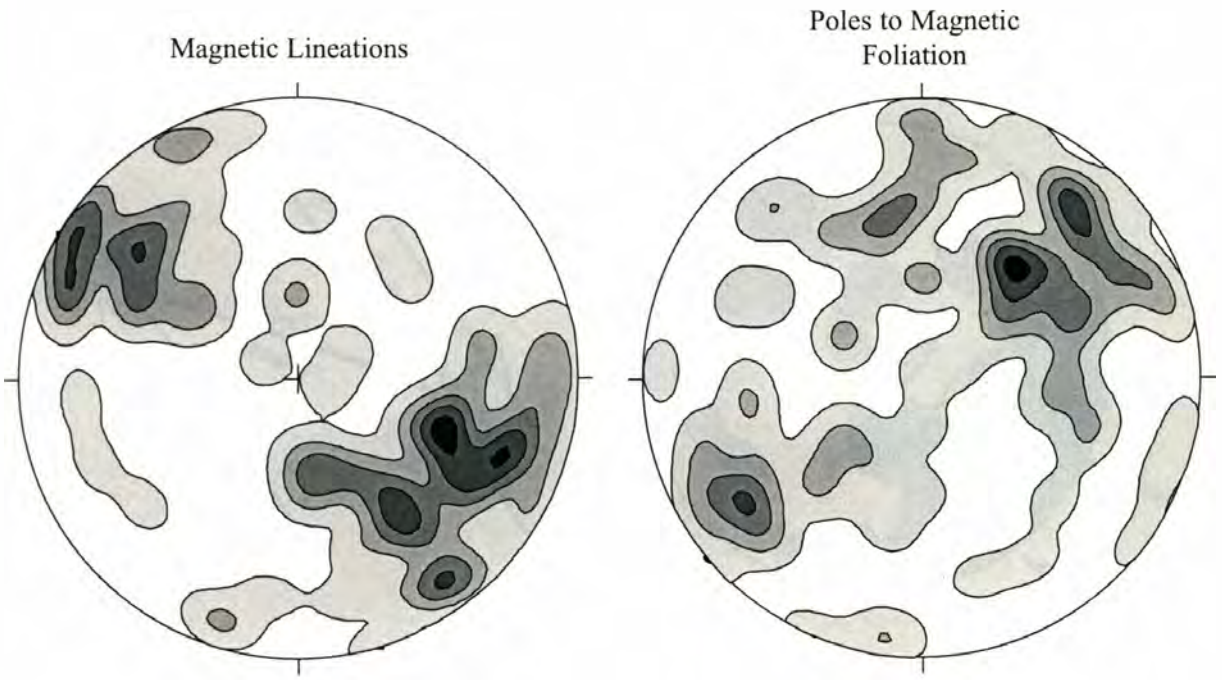

Figure 17. Contoured lower hemisphere projections of all magnetic fabrics in the Cooper Mountain pluton. The projection on the left is magnetic lineation and the projection on the right is poles the magnetic foliation.

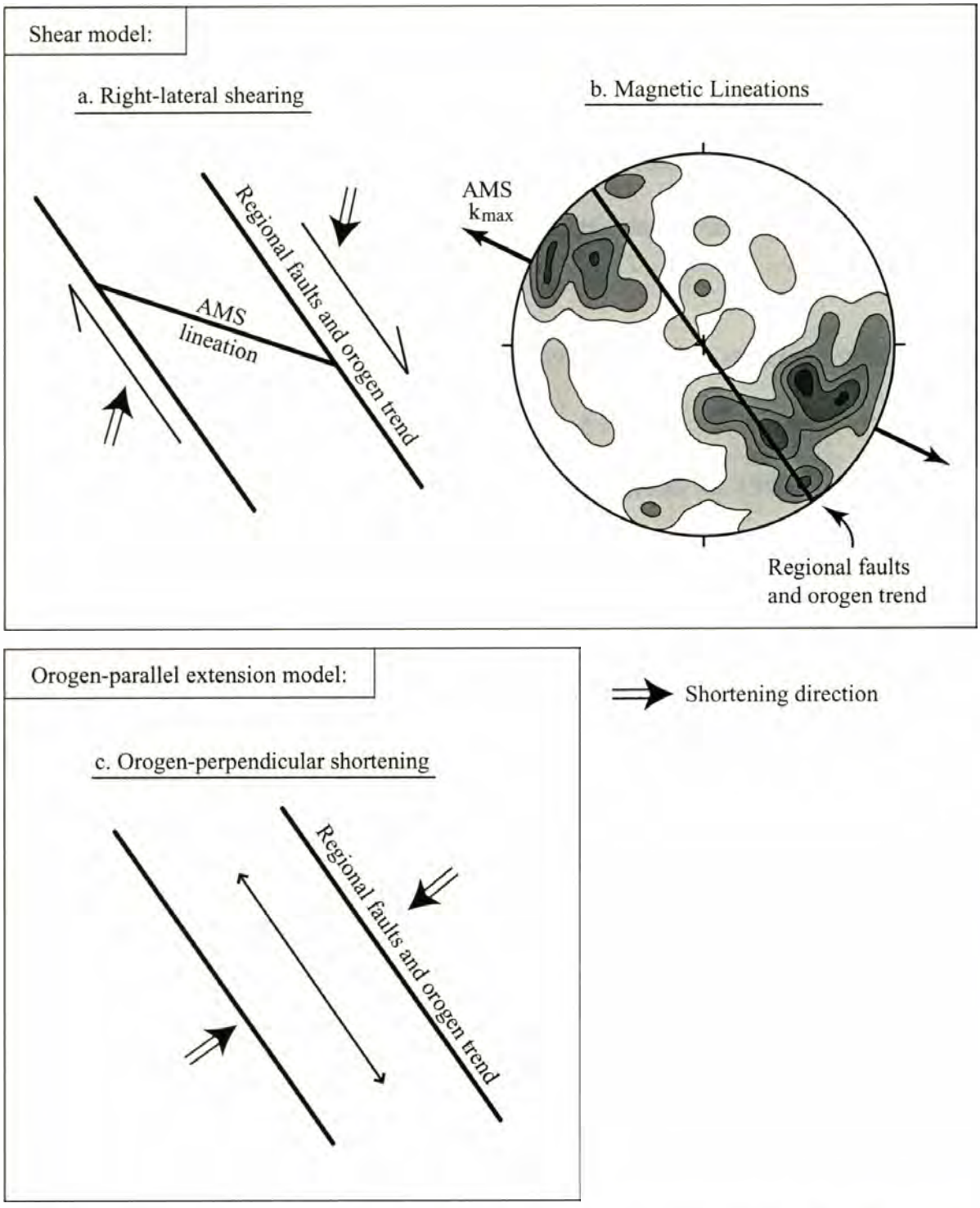

Figure 18. Two models used to explain fabric orientation. The *shear model* shows right-lateral shearing causing lineation to be oblique to the trend of the orogen and regional faults (a). Figure b is a lower-hemisphere contour of Cooper Mountain pluton magnetic lineations showing the average direction of magnetic lineation and the trend of the orogen. The *orogen-perpendicular extension model* (c) shows orogen-perpendicular shortening resulting in extension parallel to the orogen.

REFERENCES

BARKSDALE, J. D. 1975. Geology of the Methow Valley, Okanogan County, Washington. Washington Division of Geology and Earth Resources Bulletin, no. 68.

BECK, M. E., JR. 1999. On the shape of paleomagnetic data sets. Journal of Geophysical Research, 104: 25,427-25,441.

BECK, M. and NOSON, L. 1972. Anomalous paleolatitudes in Cretaceous granitic rocks. Nature Physical Science, 235: 11-13.

BENN, K., HAM, N. M., PIGNOTTA, G. S., and BLEEKER, W. 1998. Emplacement and deformation of granites during transpression: magnetic fabrics of the Archean Sparrow pluton, Slave Province, Canada. Journal of Structural Geology, 20: 1247-1259.

BENN, K., PATERSON, S. R., LUND, S. P., PIGNOTTA, G. S., and KRUSE, S. 2001. Magmatic fabrics in batholiths as markers of regional strains and plate kinematics: example of the Cretaceous Mt. Stuart batholith. Physical and Chemical Earth, 26: 343-354.

BORRADAILE, G. J. and HENRY, B. 1997. Tectonic applications of magnetic susceptibility and its anisotropy. Earth-Science Reviews, 42: 49-93.

BORRADAILE, G. J. and KEHLENBECK, M. M. 1996. Possible cryptic tectono-magnetic fabrics in 'post-tectonic' granitoid plutons of the Canadian Shield. Earth and Planetary Science Letters, 137: 119-127.

BOUCHEZ, J. L. 1997. Granite is never isotropic: An introduction to AMS studies of granitic rocks. *In* Granite: From Segregation of Melt to Emplacement Fabrics. *Edited by* J. L. Bouchez, D. H. W. Hutton, and W. E. Stephens, Kluwer, Boston, pp. 95-112.

BOUILLIN, J., BOUCHEZ, J., LESPINASSE, P., and PECHER, A. 1993. Granite emplacement in an extensional setting: an AMS study of the magmatic structures of Monte Capanne (Elba, Italy). Earth and Planetary Science Letters, 118: 263-279.

BROWN, E. H., and TALBOT, J. L. 1989. Orogen-parallel extension in the North Cascades Crystalline Core, Washington. Tectonics, 8: 1105-1114.

CONSTABLE, C. and TAUXE, L. 1990. The bootstrap for magnetic susceptibility tensors. Journal of Geophysical Research, 95: 8383-8395.

CRUDEN, A. R., TOBISH, O. T., LAUNEAU, P. 1999. Magnetic fabric evidence for conduit-fed emplacement of a tabular intrusion: Dinkey Creek pluton, central Sierra Nevada batholith, California. Journal of Geophysical Research, 104: 10511-10530.

DIEHL, J. F., BECK, M. E., JR., BESKE-DIEHL, S., JACOBSON, D., and HEARN, B. C., JR. 1983. Paleomagnetism of the Late Cretaceous-Early Tertiary North-Central Montana Alkalic Province. Journal of Geophysical Research, 88: 10,593-10,609.

DUNLOP, D. J. and ÖZDEMIR, Ö. 1997. Rock Magnetism, Fundamentals and Frontiers. Cambridge University Press, Cambridge: 571p.

EWING, T. E. 1980. Paleogene tectonic evolution of the Pacific Northwest. The Journal of Geology, 88: 619-638.

FISHER, R. A. 1953. Dispersion on a sphere. Proceedings of the Royal Society of London, 217: 295-305.

HAUGERUD, R. A., BROWN, E. H., TABOR, R. W., KRIENS, B. J., and McGRODER, M. F. 1994. Late Cretaceous and early Tertiary orogeny in the North Cascades. *In* Geologic Field Trips in the Pacific Northwest: 1994 Geological Society of

America Annual Meeting. *Edited by* D. A. Swanson and R. A. Haugerud, Department of Geological Sciences, University of Washington, Seattle, pp. 2E-1 - 2E-29.

HAUGERUD, R. A., MILLER, R. B., TABOR, R. W. and PHILLIPS, W. M. 1991a. Ross Lake Fault near Gabriel Peak, North Cascades Range, Washington [abstract]. Geological Society of America, Abstracts with Programs, 23: 34.

HAUGERUD, R. A., VAN DER HEYDEN, P., TABOR, R. W., STACEY, J. S., and ZARTMAN, R. E. 1991b. Late Cretaceous and early Tertiary plutonism and deformation in the Skagit Gneiss Complex, North Cascade Range, Washington and British Columbia. Geological Society of America Bulletin, 103: 1297-1307.

HOPSON, C. A. and MATTINSON, J. M. 1994. Chelan Migmatite Complex, Washington: Field evidence for mafic magmatism, crustal anatexis, mixing and protodiapiric emplacement. From: Swanson, D. A. and Haugerud, R. A. (editors), Geological Field Trips in the Pacific Northwest: 1994 Geological Society of America Annual Meeting: 2KMAX-21.

HOPSON, C. A. and MATTINSON, J. M. 1999. Birth of an epizonal Mid-Eocene granitoid pluton from the Late Cretaceous – Early Tertiary Skagit Gneiss Complex, North Cascades, Washington [abstract]. Geological Society of America, Abstracts with Programs, 31: A-63.

HROUDA, F. 1982. Magnetic Anisotropy of rocks and its application in geology and geophysics. Geophysical Surveys, 5: 37-82.

HROUDA, F. 1994. A technique for the measurement of thermal changes of magnetic susceptibility of weakly magnetic rocks by the CS-2 apparatus and KLY-2 Kappabridge. Geophysical Journal International, 118: 604-612.

HROUDA, F. and JELINEK, V. 1990. Resolution of ferromagnetic and paramagnetic anisotropies in rocks, using combined low-field and high-field measurements. Geophysical Journal International, 103: 75-84.

HROUDA, F., JELINEK, V., and ZAPLETAL, K. 1997. Refined technique for susceptibility resolution into ferromagnetic and paramagnetic components based on susceptibility temperature-variation measurement. Geophysical Journal International, 129: 715-719.

JELINEK, V. 1981. Characterization of the magnetic fabric of rocks. Tectonophysics, 79: T63-T67.

KIRSCHVINK, J. K. 1980. The least-squares line and plane and the analysis of paleomagnetic data. Geophysical Journal of the Royal Astronomical Society, 62: 699-718.

KRIENS, B. and WERNICKE, B. 1990. Nature of the contact zone between the North Cascades Crystalline Core and the Methow sequence in the Ross Lake area, Washington: Implications for Cordilleran tectonics. Tectonics, 9: 953-981.

LOWRIE, W. 1990. Identification of ferromagnetic minerals in a rock by coercivity and unblocking temperature properties. Geophysical Research Letters, 17: 159-162.

MATTINSON, J. M. 1972. Age of zircons from the Northern Cascade Mountains, Washington. Geological Society of America Bulletin, 83: 3769-3784.

McNULTY, B. A., TOBISCH, O. T., CRUDEN, A. R., and GILDER, S. 2000. Multistage emplacement of the Mount Givens pluton, central Sierra Nevada batholith, California. Geological Society of America Bulletin, 112: 119-135.

MILLER, R. B., PATERSON, S. R., DeBARI, S. M., and WHITNEY, D. L. 2000. North Cascades Cretaceous crustal section: Changing kinematics, rheology, metamorphism, pluton emplacement and petrogenesis from 0 to 40 kilometres depth. *In* Guidebook for Geological Field Trips in Southeastern British Columbia. *Edited by* W. H. Mathews, Department of Geology, University of British Columbia, Vancouver, pp. 229-278.

MISCH, P. 1966. Tectonic evolution of the Northern Cascades of Washington State. Special Volume, Canadian Institute of Minerals and Metallurgy, 8: 101-148.

NAGATA, T. 1961. Rock Magnetism, Revised Edition. Maruzen Company Limited, Tokyo: 350p.

PATERSON, S. R., FOWLER, T. K., JR., SCHMIDT, K. L., YOSHINOBU, A. S., YUAN, E. S., and MILLER, R. B. 1998. Interpreting magmatic fabric patterns in plutons. Lithos, 44: 53-82.

PATERSON, S. R. and MILLER, R. B. 1998. Magma emplacement during arc-perpendicular shortening: An example from the Cascades Crystalline Core, Washington. Tectonics, 17: 571-586.

PATERSON, S. R., VERNON, R. H., and TOBISCH, O. T. 1989. A review of criteria for the identification of magmatic and tectonic foliations in granitoids. Journal of Structural Geology, 11: 349-363.

POTTER, D. K. and STEPHENSON, A. 1988. Single-domain particles in rocks and magnetic fabric analysis. Geophysical Research Letters, 15: 1097-1100.

RAVIOLA, F. P. 1988. Metamorphism, plutonism and deformation in the Pateros-Alta Lake region, north-central Washington. San Jose State University, Masters Thesis.

TABOR, R. W., FRIZZELL, V. A., JR., WHETTEN, J. T., SWANSON, D. A., BYERLY, G. R., BOOTH, D. B., HETHERINGTON, M. J., and WAITT, R. B., JR. 1980. Preliminary geologic map of the Chelan 1:100,000 quadrangle, Washington. U. S. Geological Survey Open File Map: 80-841.

TAUXE, L. 1998. Paleomagnetic Principles and Practice. Kluwer Academic Publishers, Dordrecht: 299 p.

TIKOFF, B. and DE SAINT BLANQUAT, M. 1997. Transpressional shearing and strike-slip partitioning in the Late Cretaceous Sierra Nevada magmatic arc, California. Tectonics, 16: 442-459.

TIKOFF, B. and GREENE, D. 1997. Stretching lineations in transpressional shear zones: an example from the Sierra Nevada batholith, California. Journal of Structural Geology, 19: 29-39.

UYEDA, S., FULLER, M. D., BELSHE, J. C., and GIRDLER, R. W. 1963. Anisotropy of Magnetic Susceptibility of Rocks and Minerals. Journal of Geophysical Research, 68: 279-291.

WADE, W. M. 1988. Geology of the northern part of the Cooper Mountain Batholith, North-central Cascades, Washington. San Jose State University, Masters Thesis.

ZIJDERVELD, J. 1967. Demagnetization of rocks: Analysis of results. *In* Methods in Paleomagnetism. *Edited by* D. Collinson, K. Creer and S. Runcorn, Elsevier, New York, pp. 254-286.

APPENDIX A

FIELD AND PETROGRAPHIC OBSERVATIONS

Fieldwork for this study was done along Lake Chelan (see Figure 1), logging roads, trails and trough the brush. Many areas were tree covered and outcrops are few except for along the lake and logging roads. The margins of the Cooper Mountain pluton (CMP) are characterized by a stockwork of dikes and sills cutting Skagit Gneiss Complex foliation (Figures A.1, A.2 and 2). Blocks of Skagit Gneiss Complex with fabric discordant to the well-defined Skagit foliation were observed at the northwest margin of the pluton.

The petrography of the Cooper Mountain pluton was studied to determine lithologic variation within the body. Slabbed hand samples were stained with hydrofluoric acid to discriminate potassium-feldspar from plagioclase. Modes of these stained slabs were obtained by point-counting (Table A.1). The QAP classification is shown in Figure A.3. Figure 5 shows locations of sites for which modes were determined. No mappable lithologic distinctions could be made based on mode, but there are NE-SW trending swaths of porphyritic phase through the field area. More fieldwork needs to be done to confirm.

The Cooper Mountain pluton is granite to granodiorite with biotite and hornblende as the mafic constituents. The granite contains 30-50% quartz, 29-47% plagioclase, 16-24% potassium-feldspar and 2-8% mafic minerals. The granite is divided

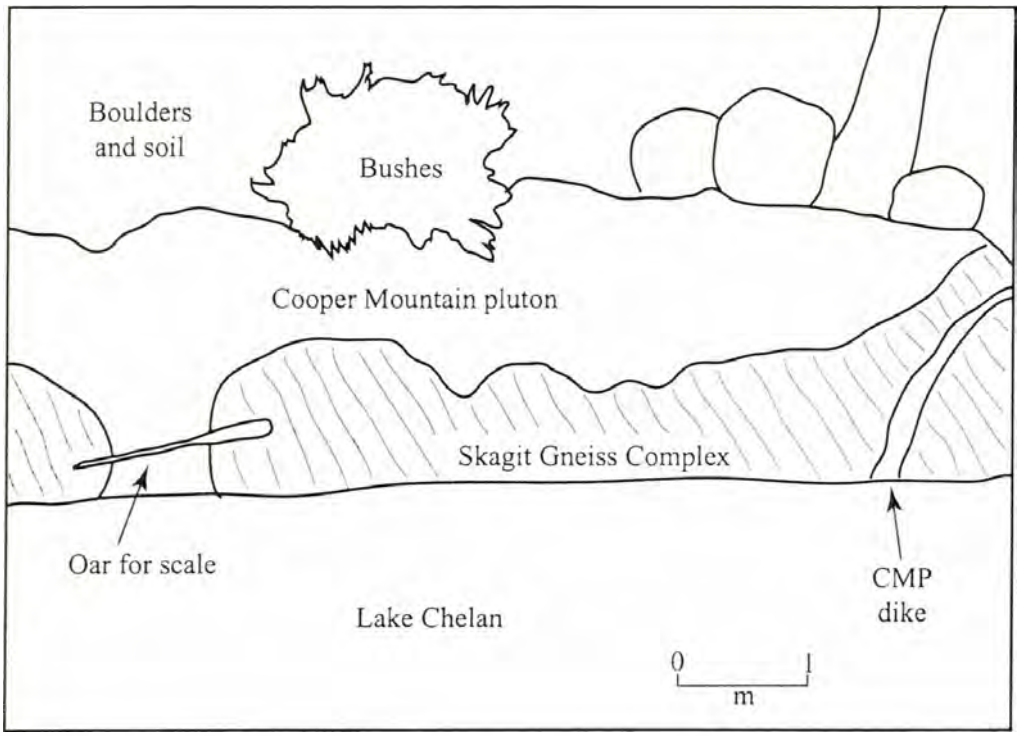

Figure A.1 Site 173; Cooper Mountain pluton (CMP) intruding Skagit Gneiss Complex (SGC). The CMP crosscuts SGC foliation. Upper image is a photograph of the site with an oar for scale; lower image is a sketch of the photograph.

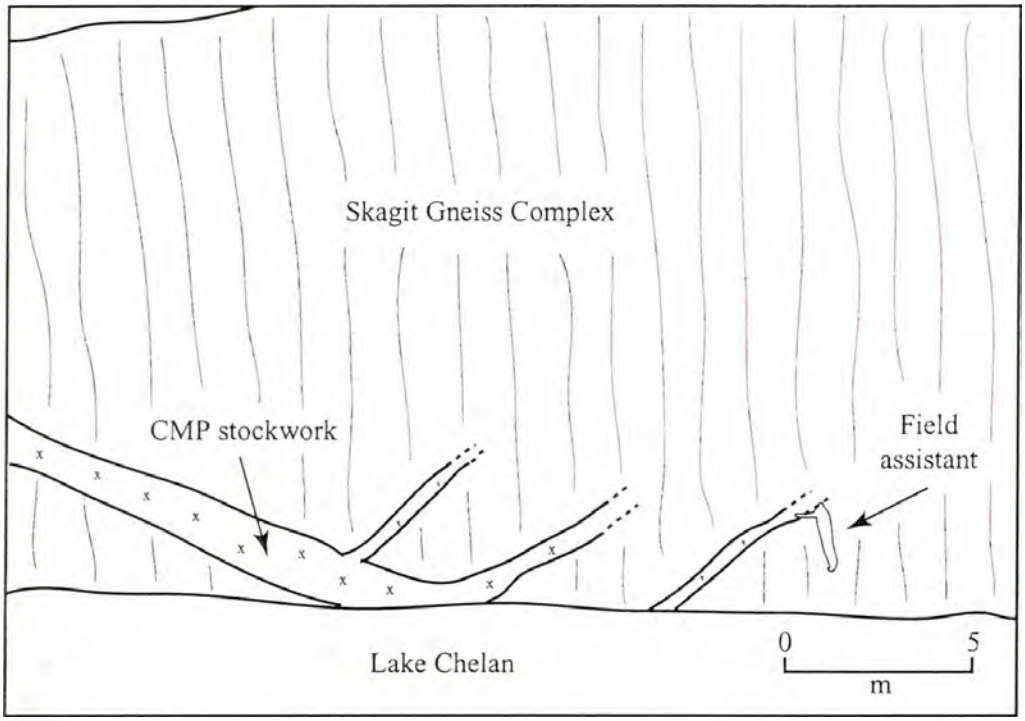

Figure A.2 Stockwork of dikes and sills (Cooper Mountain pluton, CMP) intruding the country rock (Skagit Gneiss Complex). Field assistant for scale. Upper image is a photograph of the outcrop; lower image is a sketch of the photograph.

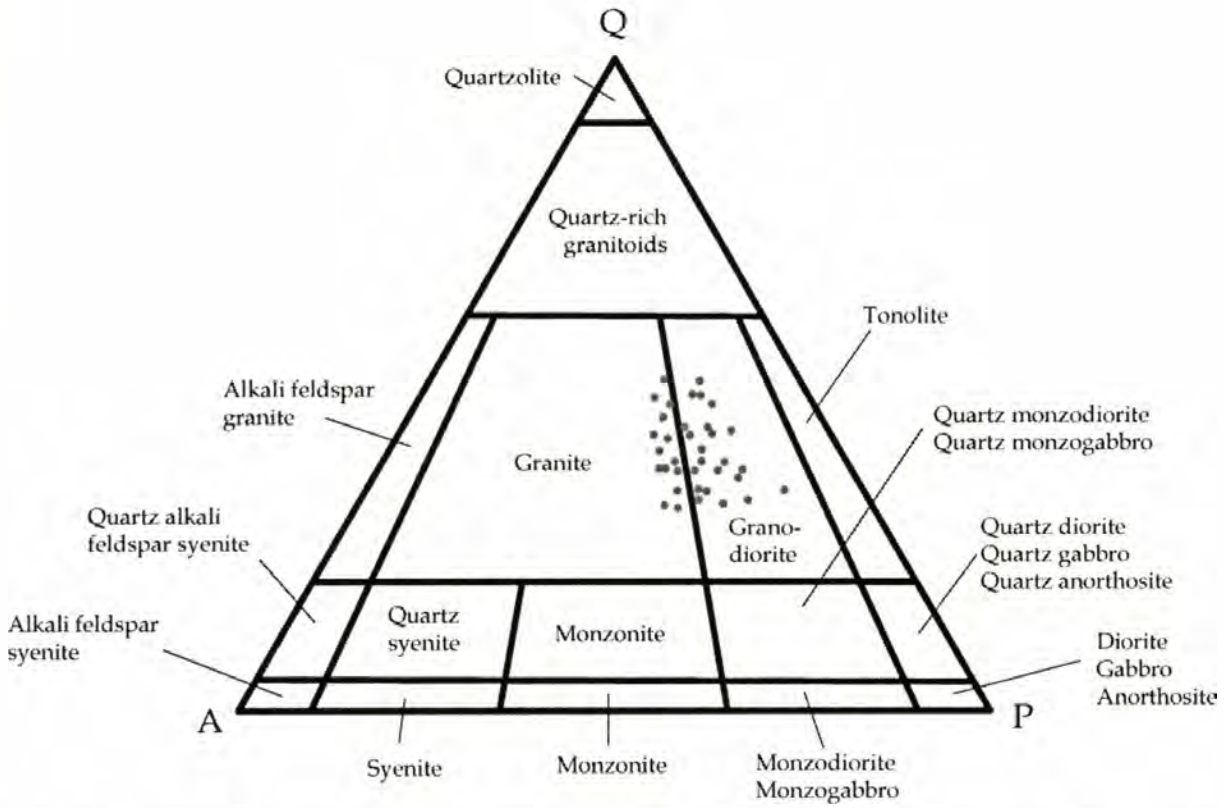

Figure A.3 QAP diagram for Cooper Mountain pluton specimens; n = 35. See Table A.1 for site numbers and raw data.

in to three groups based on grain size: porphyritic, equigranular and fine-grained granite. The porphyritic granite contains 0.1-2.0 cm subhedral potassium-feldspar phenocrysts, 0.1-0.7 cm anhedral quartz, 0.1-0.7 cm subhedral plagioclase and ≤ 0.3 cm anhedral mafics. The equigranular granite contains 0.1-0.6 cm subhedral potassium-feldspar, 0.1-0.7 cm anhedral quart z, 0.1-0.7 cm subhedral plagioclase and ≤ 0.3 cm anhedral mafics. The fine-grained granite contains subhedral plagioclase and potassium-feldspar that is ≤ 0.3 cm, anhedral quartz that is ≤ 0.2 cm and ≤ 0.3 cm anhedral mafics. Figures A.4 and A.5 are two photomicrographs of representative samples of granite. Figure A.5 shows poikilitic texture in granite.

Site number	Sample number	Quartz		Plagioclase		K-feldspar		Mafics		Total	Rock
		no.	%	no.	%	no.	%	no.	%	no.	Type
11	183-11	350	35.8	364	37.3	240	24.6	23	2.4	977	EG
12	183-12	415	41.5	334	33.4	235	23.5	16	1.6	1000	EG
49	183-25	373	37.3	334	33.4	229	22.9	64	6.4	1000	PG
72	183-46	383	40.9	397	42.4	119	12.7	37	4.0	936	FGD
84	183-57b	355	35.5	424	42.4	161	16.1	60	6.0	1000	EGD
86	183-59	345	35.3	441	45.1	139	14.2	52	5.3	977	PGD
126	183-87a	262	41.9	196	31.3	123	19.6	45	7.2	626	EG
127	183-88	334	33.4	452	45.2	149	14.9	65	6.5	1000	PGD
179	183-117	478	48.5	336	34.1	133	13.5	39	4.0	986	EGD
181	183-118	261	34.5	311	41.1	126	16.6	59	7.8	757	PGD
186	183-122	408	40.8	394	39.4	159	15.9	40	4.0	1001	FGD
188	183-124	294	35.4	301	36.3	185	22.3	50	6.0	830	EG
197	183-132b	301	40.2	266	35.5	85	11.3	97	13.0	749	PGD
224	183-153b	323	32.3	410	41.0	213	21.3	55	5.5	1001	PGD
237	183-158	294	30.2	439	45.1	182	18.7	58	6.0	973	EG
240	183-160	215	31.7	285	42.0	144	21.2	35	5.2	679	PGD
302	183-202	186	29.5	294	46.7	100	15.9	50	7.9	630	EGD
303	183-203	360	36.0	399	39.9	185	18.5	56	5.6	1000	PGD
310	183-209b	397	46.0	258	29.9	167	19.4	41	4.8	863	FG
312	183-210	391	44.6	302	34.4	126	14.4	58	6.6	877	PGD
332	183-222	409	41.0	386	38.7	158	15.8	44	4.4	997	PGD
344	183-227	301	30.1	487	48.7	93	9.3	119	11.9	1000	PGD
345	183-228	370	37.8	384	39.2	178	18.2	47	4.8	979	EGD
347	183-230	404	40.4	367	36.7	184	18.4	45	4.5	1000	EGD
353	183-234	349	34.9	359	35.9	242	24.2	50	5.0	1000	EG
360	183-241	333	33.3	401	40.1	244	24.4	22	2.2	1000	PG
363	183-244	282	35.4	318	39.9	163	20.5	33	4.1	796	PGD
366	183-247	425	45.1	307	32.6	170	18.0	40	4.2	942	EG
367	183-248	455	50.0	267	29.3	154	16.9	34	3.7	910	EG
370	183-251	360	36.0	396	39.6	223	22.3	21	2.1	1000	PG
374	183-255	303	30.3	386	38.6	262	26.2	49	4.9	1000	PG
376	183-257	382	46.6	279	34.1	124	15.1	34	4.2	819	PGD
379	183-260	354	41.4	308	36.0	161	18.8	32	3.7	855	PGD
381	183-262	269	29.1	364	39.4	226	24.5	65	7.0	924	PG
382	183-263	288	31.5	391	42.7	186	20.3	50	5.5	915	PGD

Table A.1 Modal raw data for the Cooper Mountain pluton. Site numbers correspond to sites in Figure 5. Data plotted on a QAP diagram (minus the mafics) in Figure A.3. Rock type abbreviations: PG – porphyritic granite, EG – equigranular granite, FG – fine-grained granite, PGD – porphyritic granodiorite, EGD – equigranular granodiorite, FGD – fine-grained granodiorite.

The granodiorite is comprised of 29-47% quartz, 33-48% plagioclase, 9-26% potassium-feldspar and 2-13% mafics (see Table A.1). The mafic minerals are biotite and hornblende. The granodiorite is divided into three groups much like the granite. The porphyritic granodiorite has 0.1-1.7 cm subhedral potassium-feldspar phenocrysts, 0.1-1.2 cm subhedral plagioclase, 0.1-0.5 cm anhedral quartz and ≤ 0.4 cm mafics. The equigranular granodiorite contains 0.1-0.8 cm subhedral potassium-feldspar, 0.1-1.0 cm subhedral plagioclase, 0.1-0.7 cm anhedral quartz and ≤ 0.3 cm mafics. The fine-grained granodiorite contains ≤ 0.4 cm subhedral potassium-feldspar, subhedral plagioclase and anhedral quartz that is ≤ 0.3, and ≤ 0.2 cm mafics. Figure A.6 is a photomicrograph of a representative sample of granodiorite.

Accessory minerals constitute less than 1% of the modal composition of both rock types and include apatite, zircon and opaques. Reflected light microscopy identified ilmenite and magnetite as the opaque minerals. Figures A.7 and A.8 contain two photomicrographs of opaque iron-oxides. Minor chlorite is found in both the granite and granodiorite. Chlorite is found in veins and replacing biotite (see Figure A.9). Minor epidote is found with chlorite (< 0.1% of modal composition).

Most of the quartz in both rock types occurs as anhedral grains, some of which have undergone static recrystallization. These recrystallized grains have serrated grain boundaries, are restricted to the pluton margins and lack pervasive stress features (see Figure A.10).

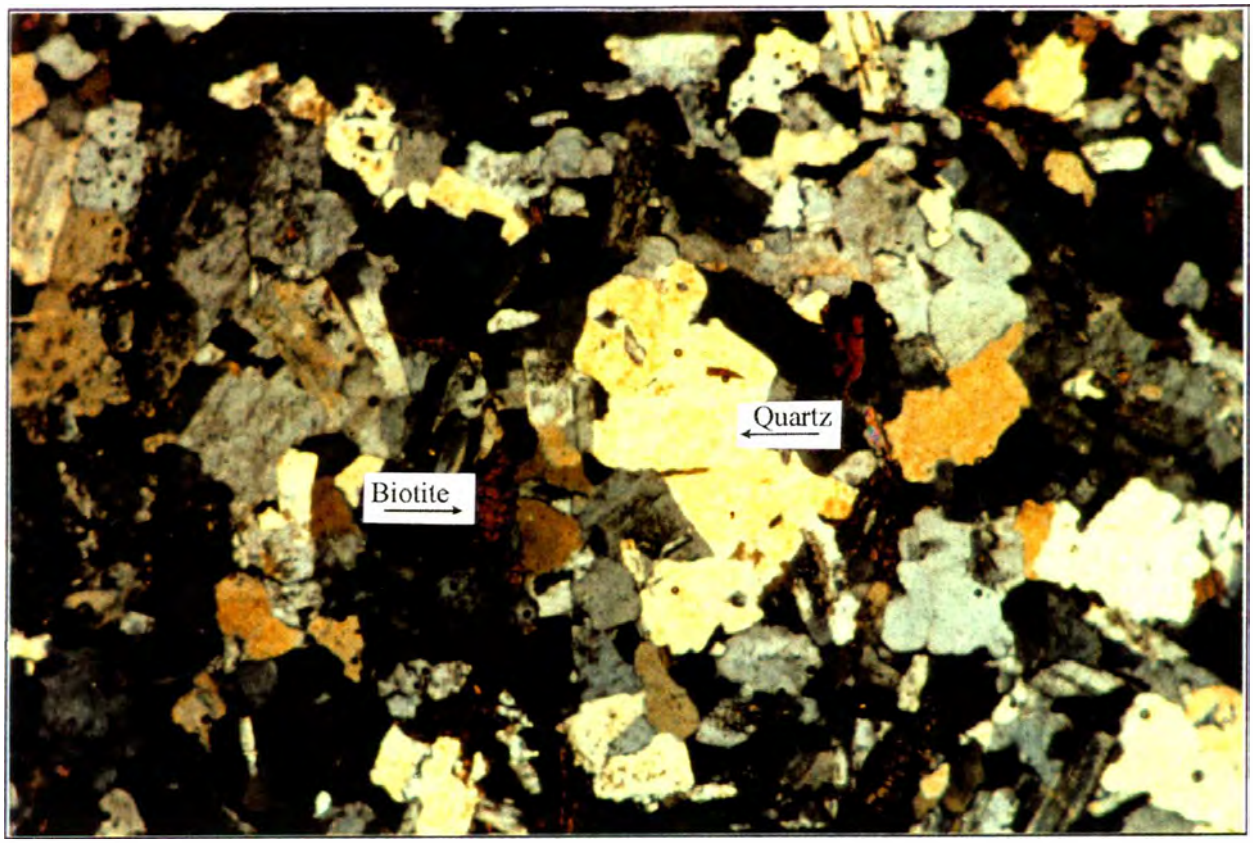

Figure A.4 Sample 183-117, equigranular granite. Undeformed quartz grains and randomly oriented biotite grains. $k = 8.01 \times 10^{-5}$, P = 1.0712, T = -0.0772. Image in cross-polarized light. Scale = 20x magnification; 3.4 x 5.1 mm.

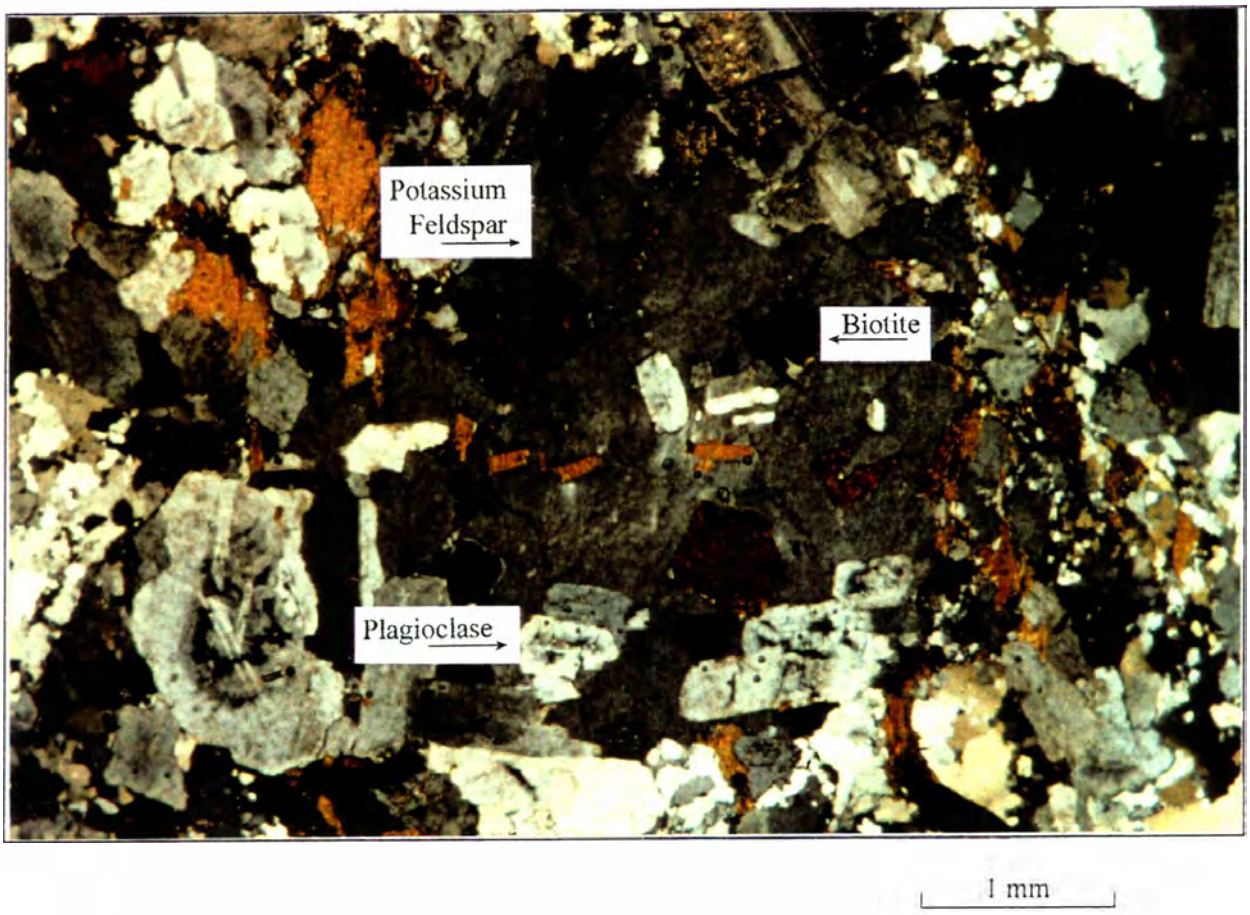

Figure A.5 Sample 183-262, porphyritic granite. Poikilitic texture (biotite and plagioclase grains within potassium feldspar). Image in cross-polarized light. Scale = 16x magnification; 4.2 x 6.4 mm.

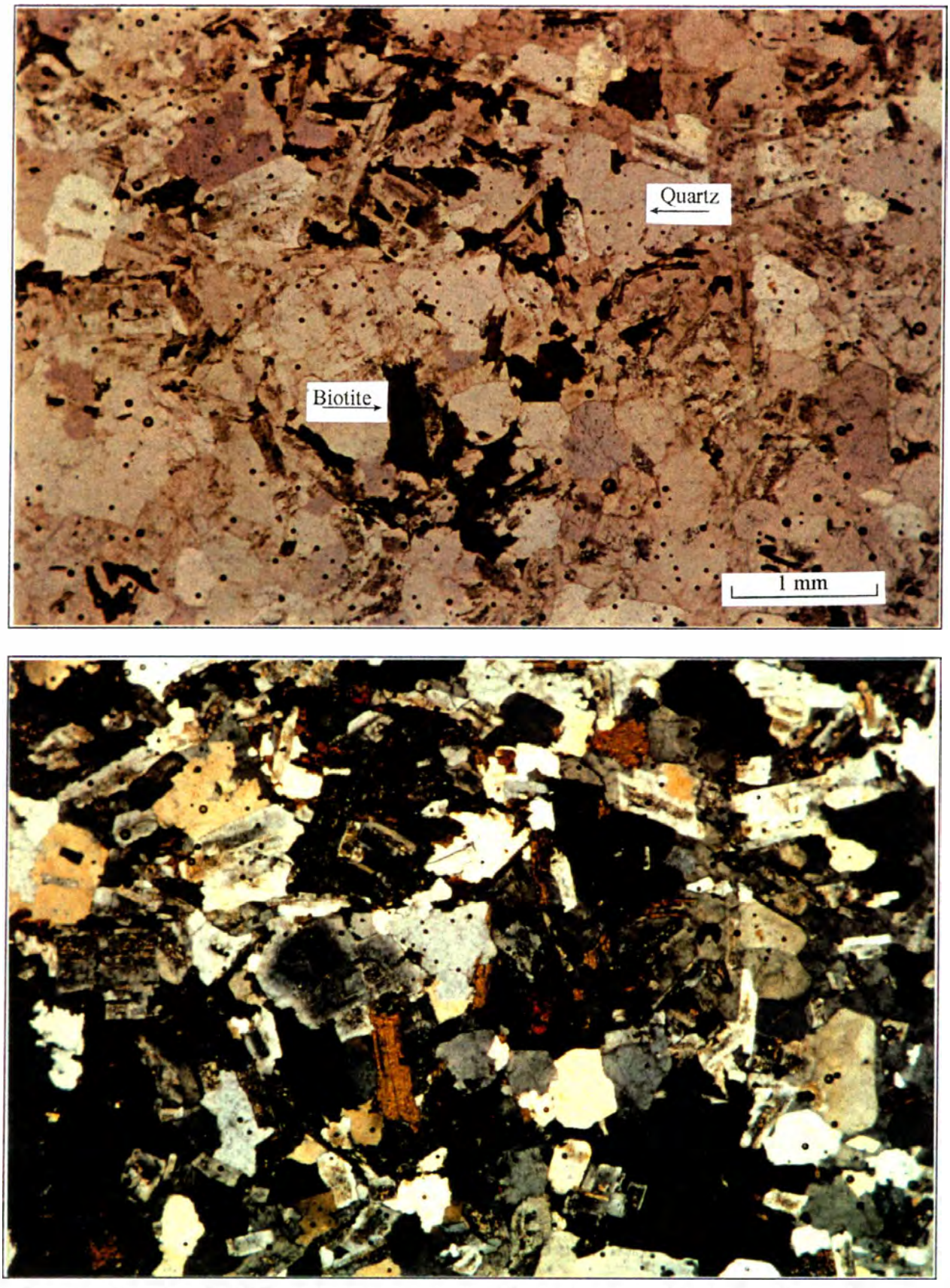

Figure A.6 Sample 183-257, porphyritic granodiorite. Randomly oriented biotites, undeformed quartz, some sauceritization. $k = 9.19 \times 10^{-5}$, P = 1.0435, T = 0.479. Upper image in plane-polarized light, lower image in cross-polarized light. Scale = 16x magnification; 4.2 x 6.4 mm.

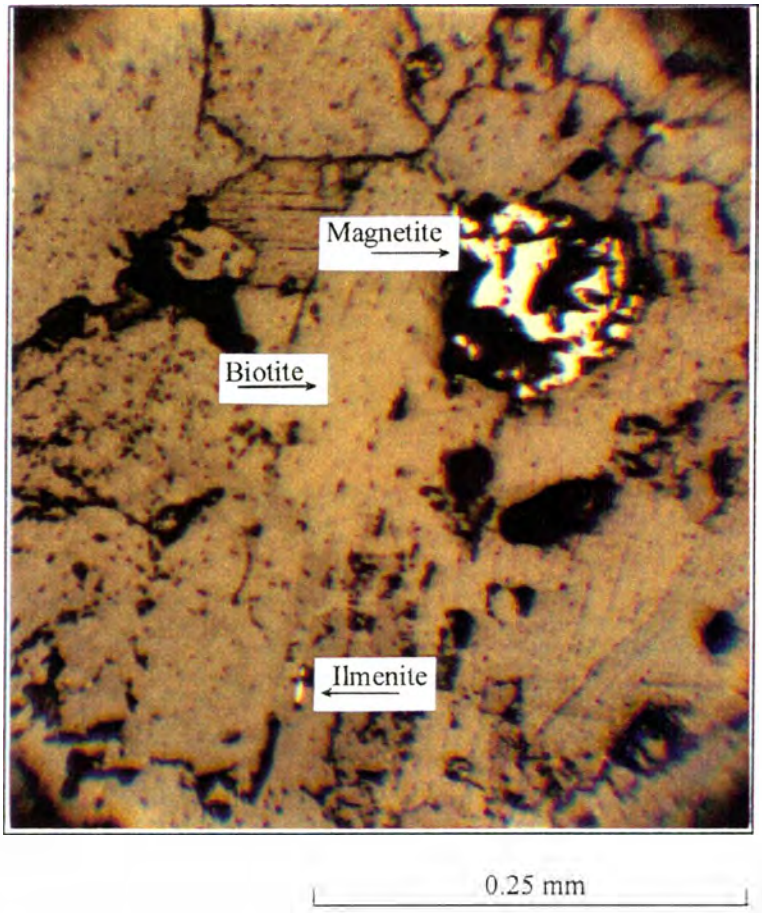

Figure A.7 Sample 183-247. Reflected light image showing magnetite and ilmenite grains within a biotite grain. Scale = 8x magnification.

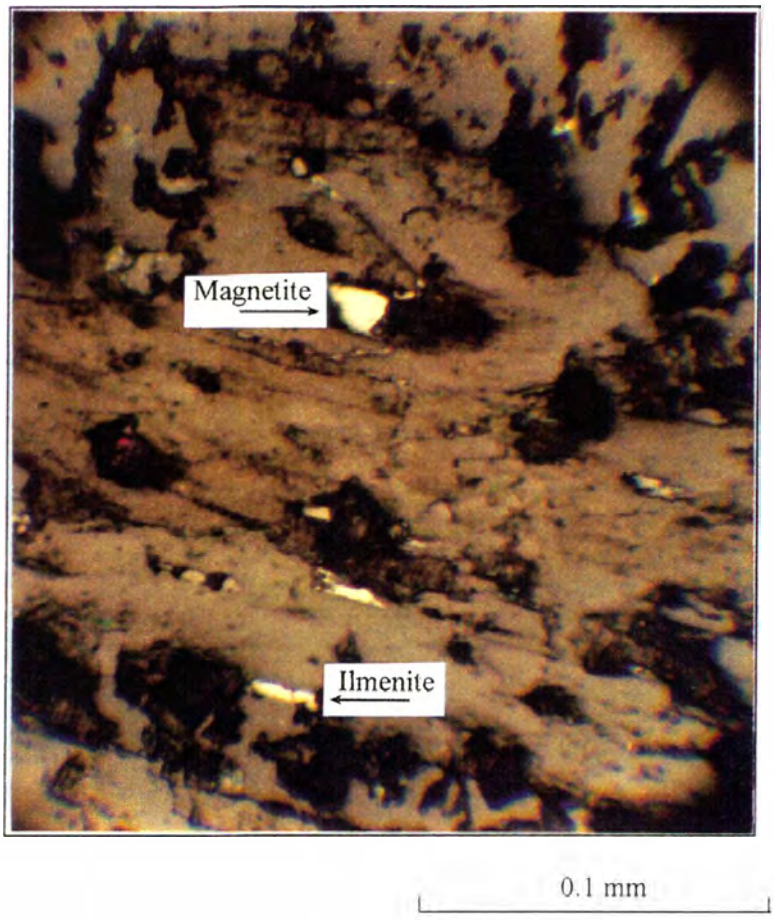

Figure A.8 Sample 183-2. Reflected light image showing magnetite and ilmenite grains within a biotite grain. Scale = 16x magnification.

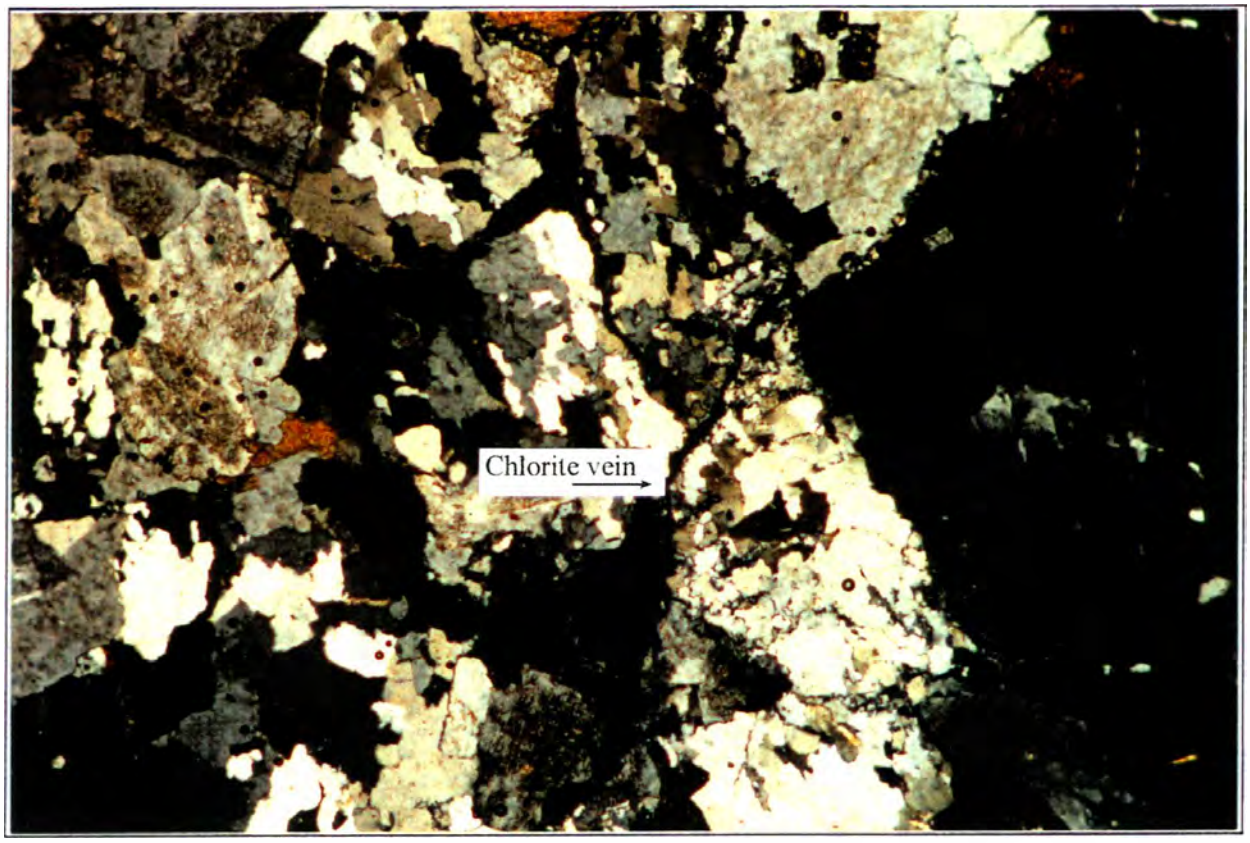

Figure A.9 Sample 183-244, porphyritic granite. Streaked-out, recrystallized quartz in a shear zone. Veins filled with chlorite or chlorite replacing biotite. $k = 8.49 \times 10^{-5}$, P = 1.0664, T = 0.078. Image in cross-polarized light. Scale = 25x magnification; 2.7 x 4.1 mm.

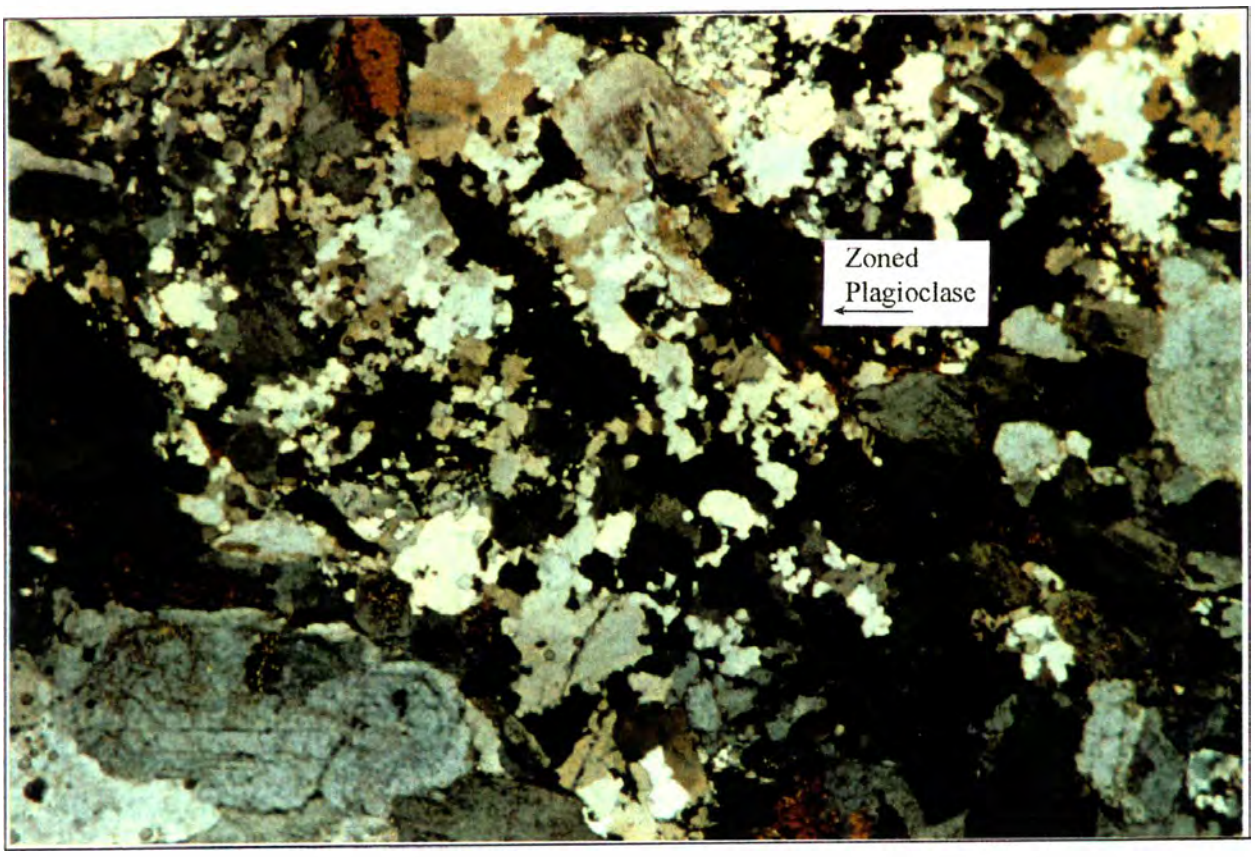

Figure A.10 Sample 183-262, porphyritic granite. Subgrain development in quartz. Quartz-subgrains not stretched out, no alignment. Zoned plagioclase grain northeast of center. Thin section cut parallel to magnetic lineation. $k = 9.68 \times 10^{-5}$. Image in cross-polarized light. Scale = 16x magnification; 4.2 x 6.4 mm.

APPENDIX B

ANISOTROPY OF MAGNETIC SUSCEPTIBILITY (AMS)

SAMPLE COLLECTION AND MACHINE SPECIFICATIONS

Oriented hand samples were collected from 113 sites in the field and drilled in the lab. One to five cores (average 2) were drilled per hand sample with one to three specimens cut (average 2) per core. Note: the core orientation line was drawn directly on the brass scribe-line and individual specimens from each core were labeled *a*, *b*, and *c* with *a* being the specimen farthest out of the outcrop and *c* being the specimen farthest in the outcrop. The Kappabridge KLY-3 was used to measure the AMS. Specifications: field intensity = 300 Am^{-1}, sensitivity = 3 x 10^{-8} (SI) (for bulk susceptibility), 2 x 10^{-8} (SI) (for a spinning specimen). AMS raw data is included on the accompanying compact disc as *.asc* files organized by site number.

STATISTICAL ANALYSIS

F-statistics

F-statistics were calculated on each specimen to determine the significance of any anisotropy. The equations and methods are explained in Tauxe (1998). Specimens 72-c1-a and 243-c1-b were omitted from further analysis because their F-values were within the 95% confidence level for isotropy meaning they had no statistically meaningful fabric.

Bootstrap Statistics

The statistically anisotropic specimens were analyzed using a bootstrap procedure to determine the degree in the orientations of the AMS data (Constable and Tauxe 1990). The scatter relates to the shape of the AMS ellipsoid, which indicates preferred crystal orientation within the rock. The AMS ellipsoid is defined along three axes of susceptibility. The axes of maximum, intermediate and minimum axes of susceptibility (k) are denoted throughout the text as k_{max}, k_{int} and k_{min}, respectively. If all three axes of susceptibility are distinct ($k_{max}>k_{int}>k_{min}$) the shape of the AMS ellipsoid is triaxial. For prolate ($k_{max}>k_{int}\approx k_{min}$) and oblate ($k_{max}\approx k_{int}>k_{min}$) shapes, an overlap in the directions between two of the three axes makes mineral orientation difficult to distinguish. Figure B.1 shows examples of sites with triaxial, prolate and oblate ellipses. The lower-hemisphere equal-area plots show the mean axes of susceptibility for a site with corresponding, statistical bootstrapped 95% confidence ellipses. Notice how Figures B.1c and B.1e have overlap in their confidence ellipses. This indicates that those axes are not statistically distinct from each other. This is important when interpreting the data, because those axes of susceptibility describe bulk mineral orientation. In addition, statistical bootstrap analysis can be interpreted with histograms. Figure B.1 includes histrograms of eigenvalues (τ) plotted against fraction of bulk susceptibility. Bars of 95% confidence are drawn above each histogram. Eigenvalues (τ_{max}, τ_{int}, τ_{min}) directly relate to eigenvectors (k_{max}, k_{int}, k_{min}), so overlap in the 95% confidence bars of the histograms suggests statistically indistinct data. When interpreting data, magnetic foliations were plotted as the k_{max}-k_{int} plane and lineations were plotted as k_{max}. Therefore, for uniaxial oblate sites, only foliations were included in the analysis, and for

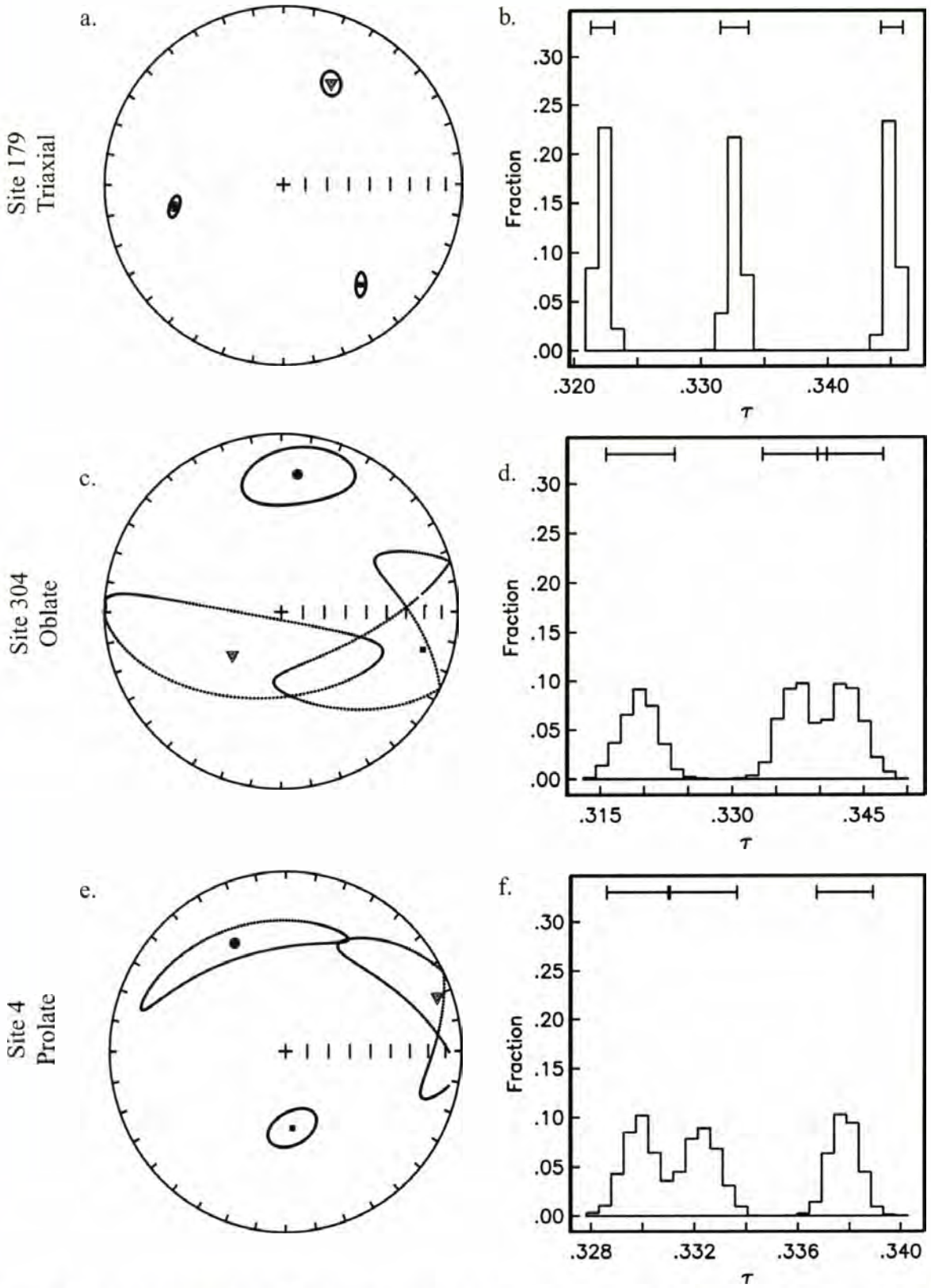

Figure B.1 Bootstrap statistical analysis lower hemisphere stereonets and histograms. Figures a, c and e: squares = k_{max} mean eigenvector, triangles = k_{int} mean eigenvector, circles = k_{min} mean eigen-vector; bootstrapped error ellipses surround each axis. Figures b, d and f: Fraction = fraction of bulksusceptibility, τ = eigenvalue; bootstrapped 95% confidence bars above each histogram.

Site No.	Sample No.	Shape	kmax	kint	kmin	bulk k
2	2	triaxial	161.4, 63.1	50.8, 10.1	316.1, 24.6	7.28E-05
3	3	oblate	169.0, 13.4	73.8, 20.8	289.7, 64.9	9.42E-05
4	4	prolate	174.7, 54.8	70.8, 9.6	334.4, 33.5	6.43E-05
10	10	triaxial	306.4, 32.3	190.8, 34.3	67.2, 39.1	1.12E-04
48	24	sphere	113.5, 6.5	18.4, 37.9	211.6, 51.4	5.10E-05
49	25	triaxial	119.5, 35.9	226.4, 21.9	341.1, 46.0	1.06E-04
50	26	sphere	141.4, 34.1	257.4, 32.9	18.6, 38.7	1.70E-04
52	28	triaxial	246.7, 23.5	154.5, 4.9	53.5, 65.9	4.68E-05
56	31	triaxial	3.7, 40.4	246.7, 28.1	133.2, 36.7	5.97E-05
57	32	triaxial	102.5, 23.6	227.7, 52.9	359.7, 26.9	7.06E-05
60	35	triaxial	33.8, 39.3	222.0, 50.4	127.1, 4.0	7.89E-05
61	36	triaxial	114.0, 23.7	303.5, 66.0	205.6, 3.5	8.74E-05
62	37	triaxial	98.6, 36.7	284.1, 53.2	190.5, 2.6	1.02E-04
63	38	triaxial	333.2, 17.4	79.9, 42.5	226.7, 42.4	1.27E-04
66	41b	sphere	139.8, 18.1	284.6, 68.2	45.9, 11.7	2.79E-05
72	46	triaxial	99.5, 45.7	261.1, 42.8	359.8, 9.3	1.14E-04
73	47	sphere	61.6, 33.3	190.3, 43.6	311.0, 28.2	7.57E-05
74	48ab	triaxial	86.3, 37.0	198.7, 26.9	315.1, 41.2	6.99E-05
75	49b	triaxial	294.8, 8.2	197.0, 43.2	33.2, 45.6	1.01E-04
76	50	triaxial	81.7, 3.0	174.2, 40.2	348.1, 49.6	9.40E-05
80	54	triaxial	329.1, 2.3	237.3, 37.0	62.1, 52.9	1.60E-04
81	54a	triaxial	291.0, 12.7	189.5, 41.6	34.4, 45.7	1.03E-04
82	55ab	triaxial	121.0, 6.2	213.9, 24.8	17.9, 64.3	8.59E-05
83	56ab	triaxial	287.9, 16.4	184.2, 38.9	36.0, 46.5	8.43E-05
85	58	triaxial	91.6, 15.8	198.9, 46.3	348.2, 39.4	1.14E-04
86	59	triaxial	91.4, 3.2	185.5, 51.6	358.9, 38.2	1.04E-04
95	65	triaxial	335.5, 6.6	219.5, 75.1	66.8, 13.3	1.00E-04
97	66	triaxial	144.3, 13.9	13.5, 69.3	238.2, 15.0	1.34E-04
101	68	triaxial	94.2, 17.1	311.8, 68.8	188.0, 12.1	1.72E-05
102	69	prolate	106.5, 19.9	217.3, 44.6	359.6, 38.7	1.42E-04
112	75	triaxial	199.0, 13.5	300.8, 40.3	94.3, 46.6	6.30E-05
114	76	triaxial	113.9, 25.0	248.1, 56.2	13.4, 21.2	1.03E-04
122	83	triaxial	327.2, 18.5	208.7, 54.9	67.7, 28.6	6.91E-05
123	84	triaxial	311.1, 27.3	201.1, 33.6	71.1, 44.1	6.08E-05
124	85	triaxial	319.5, 25.6	182.4, 56.8	59.4, 19.7	2.10E-04
125	86ab	triaxial	306.8, 21.0	193.1, 46.2	53.2, 36.3	7.16E-05
127	88	triaxial	306.2, 5.5	212.1, 36.7	43.5, 52.7	1.09E-04
128	89	triaxial	323.6, 1.2	229.4, 73.9	54.0, 16.1	1.21E-04
176	114	triaxial	254.7, 87.4	12.5, 1.2	102.5, 2.3	6.73E-05
178	116	triaxial	126.4, 25.7	35.5, 1.9	301.5, 64.2	6.87E-05
179	117	triaxial	141.9, 30.3	25.3, 37.4	258.9, 37.8	8.01E-05
181	118	triaxial	298.3, 6.0	29.6, 12.0	182.2, 76.6	9.51E-05
182	119b	prolate	137.3, 4.6	46.3, 12.3	247.3, 76.8	8.18E-05
184	120	oblate	92.2, 17.8	354.0, 23.9	215.3, 59.5	3.55E-05
185	121	prolate	104.8, 41.6	215.1, 21.4	324.8, 40.8	8.57E-05
187	123	triaxial	105.5, 24.4	360.0, 30.5	227.1, 49.1	8.09E-05

Site No.	Sample No.	Shape	kmax	kint	kmin	bulk k
188	124	triaxial	105.8, 45.1	351.4, 22.4	243.6, 36.4	1.29E-04
189	125	prolate	104.9, 80.5	235.1, 6.2	325.9, 7.2	1.27E-04
190	126b	triaxial	143.7, 57.0	315.6, 32.7	48.0, 3.7	1.40E-04
192	128	triaxial	167.4, 64.1	5.9, 24.8	272.6, 7.3	9.59E-05
199	133a	triaxial	73.0, 31.0	338.2, 8.0	235.3, 57.8	7.87E-05
200	134a	triaxial	48.3, 45.4	161.3, 21.1	268.2, 37.1	7.58E-05
202	135	*	121.0, 27.0	349.0, 52.0	224.0, 24.0	1.01E-04
205	137a	triaxial	144.3, 11.5	256.6, 61.8	48.8, 25.4	7.19E-05
209	139	prolate	123.6, 46.6	325.5, 41.3	225.6, 11.1	8.92E-05
213	142	triaxial	231.1, 19.2	133.9, 20.0	1.5, 61.7	1.34E-04
214	143	triaxial	154.3, 37.0	339.0, 52.7	247.0, 2.0	1.66E-04
236	157b	sphere	14.2, 69.9	118.6, 5.2	210.4, 19.4	1.19E-04
240	160	triaxial	142.5, 47.6	351.6, 38.6	249.4, 14.9	1.09E-04
300	200	triaxial	114.3, 8.2	251.7, 78.9	23.2, 7.4	8.80E-05
301	201	triaxial	177.8, 67.5	50.9, 14.0	316.4, 17.3	1.49E-04
302	202	triaxial	300.4, 34.0	156.0, 50.3	43.0, 17.9	1.39E-04
303	203	triaxial	295.7, 35.5	148.9, 49.5	38.2, 16.8	7.40E-05
304	204ab	oblate	104.8, 17.9	228.8, 59.9	6.8, 23.3	8.87E-05
305	205	oblate	307.0, 51.4	209.0, 6.3	114.1, 37.9	2.14E-04
306	206	triaxial	106.2, 17.3	10.0, 19.1	235.4, 63.8	1.02E-04
308	208	triaxial	291.0, 12.0	28.4, 31.0	182.4, 56.3	2.76E-04
310	209b	triaxial	187.6, 23.2	286.4, 19.6	52.0, 58.6	6.29E-05
312	210	triaxial	143.6, 8.7	242.9, 46.7	45.7, 42.0	1.46E-04
313	211	triaxial	163.3, 1.2	253.5, 11.6	67.3, 78.4	3.86E-05
316	213	triaxial	153.0, 17.8	260.5, 43.2	46.6, 41.5	6.02E-05
318	214	triaxial	297.0, 11.5	200.2, 30.3	45.4, 57.2	2.09E-04
320	215	triaxial	110.0, 45.4	221.7, 20.0	328.1, 37.8	1.75E-04
321	216	*	307.0, 23.0	56.0, 37.0	192.0, 44.0	1.19E-04
322	217	triaxial	267.5, 26.8	112.1, 60.9	2.8, 10.4	2.16E-04
325	219a	oblate	5.4, 59.7	246.2, 15.9	148.6, 25.0	7.68E-05
327	220	triaxial	306.1, 56.5	64.6, 17.5	164.1, 27.5	1.16E-04
345	228	triaxial	331.1, 27.7	181.0, 58.8	68.2, 13.2	8.73E-05
346	229	triaxial	358.8, 67.6	203.5, 20.5	110.2, 8.7	7.59E-05
347	230	triaxial	300.6, 1.0	31.0, 24.8	208.4, 65.2	7.70E-05
353	234	triaxial	305.1, 32.9	207.9, 11.0	101.8, 54.8	1.00E-04
354	235	triaxial	315.1, 33.0	180.7, 47.1	62.0, 24.0	8.77E-05
355	236	triaxial	295.3, 52.8	198.2, 5.3	104.2, 36.6	8.87E-05
358	239	triaxial	359.7, 62.5	193.9, 26.7	101.0, 5.8	7.84E-05
360	241	oblate	303.5, 16.9	177.2, 62.8	40.1, 20.6	6.64E-04
362	243	oblate	156.7, 1.3	249.0, 60.0	66.0, 29.9	2.21E-05
363	244	triaxial	168.3, 21.9	328.1, 66.8	75.3, 7.2	8.49E-05
364	245	prolate	78.8, 14.3	174.5, 21.2	317.3, 64.0	1.84E-04
365	246	triaxial	146.1, 45.3	298.2, 41.1	41.1, 14.3	8.24E-05
366	247	triaxial	120.5, 35.6	347.4, 43.6	230.5, 25.4	9.75E-05
367	248	triaxial	139.1, 45.3	0.8, 36.5	253.4, 22.1	9.78E-05
368	249	triaxial	140.3, 17.4	15.2, 61.5	237.5, 21.9	1.79E-04

Site No.	Sample No.	Shape	kmax	kint	kmin	bulk k
370	251	oblate	304.6, 63.5	133.9, 26.2	42.0, 3.7	1.07E-04
371	252	triaxial	62.3, 73.9	318.2, 4.0	227.1, 15.6	1.02E-04
372	253	prolate	182.4, 62.3	333.2, 24.6	68.7, 11.9	1.13E-04
373	254	sphere	19.0, 77.6	174.1, 11.2	265.1, 5.1	1.27E-04
374	255	triaxial	110.8, 54.7	340.6, 24.6	239.1, 23.7	1.15E-04
375	256	triaxial	112.5, 50.5	205.0, 2.1	296.8, 39.4	7.92E-05
377	258	triaxial	120.8, 35.5	353.6, 40.3	234.8, 29.6	7.46E-05
378	259	triaxial	138.2, 41.7	240.2, 13.2	344.0, 45.3	3.10E-04
379	260	triaxial	153.1, 55.9	34.1, 18.2	294.1, 27.8	1.15E-04
380	261	triaxial	146.7, 36.1	282.6, 44.6	38.1, 23.6	1.06E-04
381	262	triaxial	161.0, 44.2	296.2, 36.1	45.3, 24.1	9.68E-05
382	263	triaxial	144.5, 39.3	341.3, 49.4	241.4, 8.4	9.49E-05
383	264	prolate	139.5, 29.3	341.7, 58.7	235.1, 9.9	6.40E-05
384	265d	triaxial	346.0, 9.3	248.0, 40.5	86.4, 48.0	9.64E-05

Table B.1 AMS data table. Shape = shape of the AMS ellipsoid based on bootstrap statistical analysis; k_{max} = axis of maximum susceptibility; k_{int} = axis of intermediate susceptibility; k_{min} = axis of minimum susceptibility; * = only one specimen available for this site, therefore bootstrap ellipsoids do not apply, fabric plotted directly.

uniaxial prolate sites, only lineations were included. In all, foliation data from 14 sites and lineation data from 13 sites could not be determined. Foliation, lineation and indeterminate site data are listed in Table B.1.

MAGNETIC ANISOTROPY DATA

P- (Nagata 1961) and T-parameters were used to quantify shape (Jelinek 1981). P = k_{max}/k_{min} depicts how anisotropic a sample is. T-values provide a sense of shape for the AMS ellipsoid that can be related to the strain ellipsoid (T = -1 is uniaxial prolate, T = 1 is uniaxial oblate, T = 0 is spherical). P- and T-data are in the *.asc* files with specimens grouped by site, on the accompanying compact disc. See Figure 8.

DETERMINING WHAT MINERALS CONTRIBUTE TO THE AMS

It is important to know what minerals contribute to the AMS signature of a specimen to know how the fabric orientations should be interpreted. For few minerals, such as single-domain magnetite, k_{max} corresponds to the crystallographic *short* of the mineral and k_{min} corresponds to the crystallographic *long* (just the opposite of what is expected) resulting in the fabric appearing to be inverse (Potter and Stephenson 1988). Typically, for specimens with a low magnetic susceptibility (less than $5x10^{-4}$), the paramagnetic minerals are the dominant contributors to the AMS (Hrouda and Jelinek 1990). To confirm this, a variety of experiments were performed to determine whether the AMS had a strongly paramagnetic (biotite) or ferromagnetic (magnetite) component.

Partial Anhysteritic Remanent Magnetization (pARM)

pARM can be used to determine the size range of magnetic minerals in a specimen. It is imparted to a specimen in the presence of an alternating magnetic field with a direct field applied over discreet windows (ranges) of coercivity. The D-2000 A.F. Demagnetizer was used for this procedure with a bias field of 0.1 mT. For example, large, multi-domain magnetite has a low coercivity (tens of millitesla) so when a specimen with multi-domain magnetite is subject to alternating field magnetization between, say, 20 and 10 mT, the magnetite grains will be coerced into acquiring a magnetization. However, if magnetized between, say, 100 and 80 mT the same multi-domain minerals will not acquire a magnetization. Such multi-domain magnetite grains produce fabrics in proportion to their own shapes and these fabric orientations should be interpreted as being "normal." Meaning, AMS data should be interpreted as k_{max} = lineation and k_{min} = pole to foliation. However, single-domain magnetite grains acquire magnetization over a high coercivity range (hundreds of mT up to 300 mT) and fabric orientation should be interpreted as "inverse." Meaning, AMS data should be interpreted as k_1 = pole to foliation and k_3 = lineation. A limitation of this method is that it does not determine the alignment of magnetic minerals, it only demonstrates if the minerals are present or not.

Forty-nine specimens were analyzed using this method to determine if multi-domain or single-domain magnetite grains were present. Data for these specimens are included on the accompanying compact disc. Figure B.2 is an example of specimens containing multi-domain and single-domain magnetite. In general, pARM results support a variety of magnetite sizes.

a. Specimen 114-c2-b

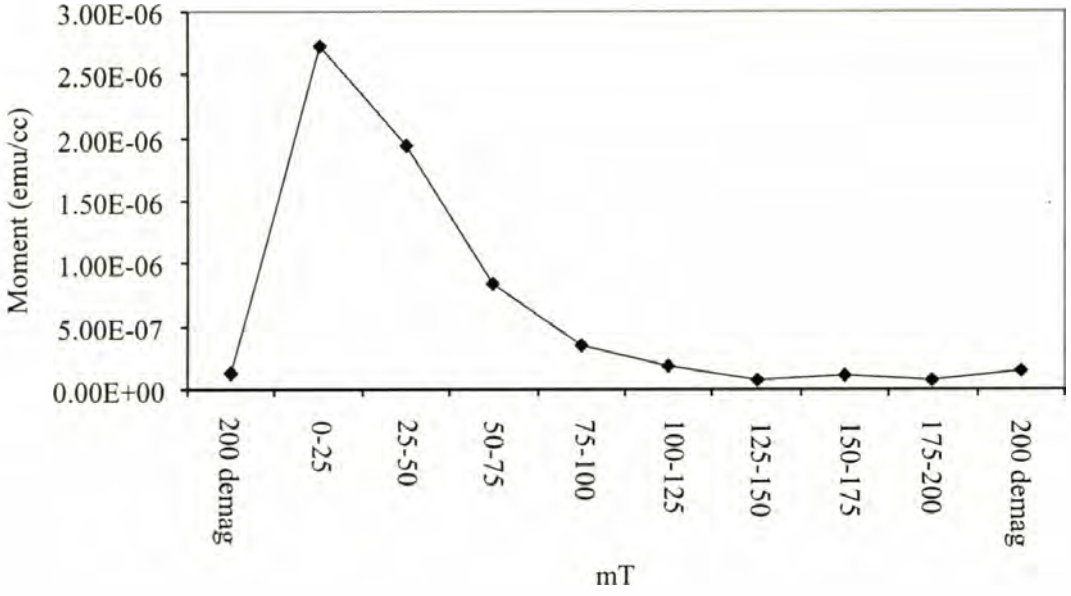

b. Specimen 258-c2-a

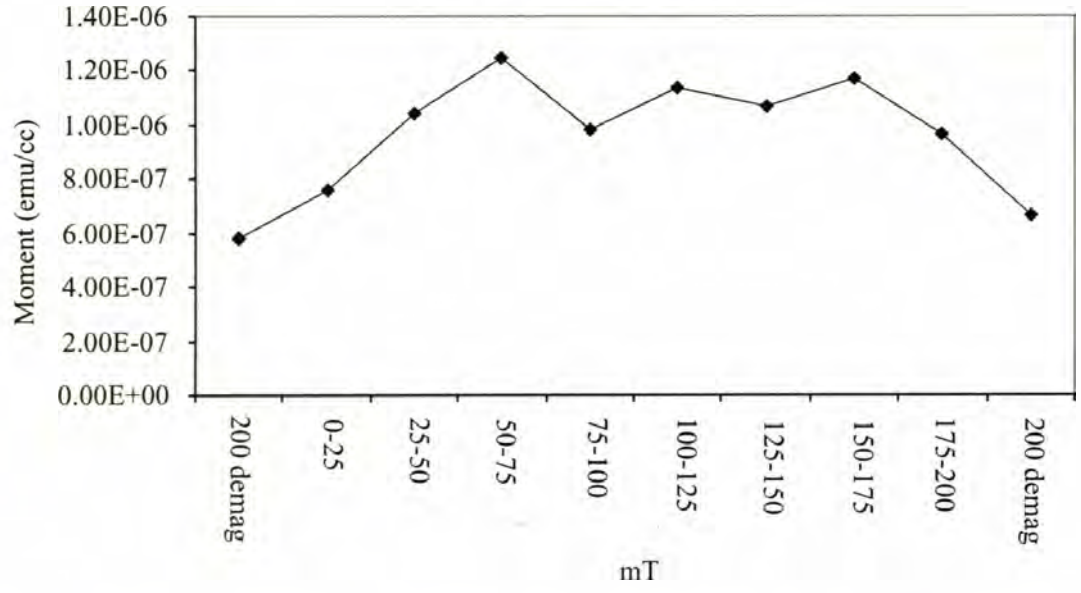

Figure B.2 Two pARM specimens. The x-axis is magnetization windows in mT; 200 demag = the specimen was demagnetized to 200 mT. The y-axis is magnetic moment.

Anhysteritic Remanent Magnetization (ARM)

ARM measurements were made to determine ferromagnetic mineral alignment. Specimens were demagnetized along +z, +y and +x axes at 200 mT with an alternating-field (AF) machine to remove most remanent magnetic field. Then each specimen was magnetized with a bias field of 0.1 mT applied over an alternating field of 200 mT in nine different orientations, with remanence measured after each magnetization. Limitations of this method involve using the D-2000 A.F. Demagnetizer. The D-2000 A.F. Demagnetizer can only magnetize and demagnetize specimens to 200 mT while some minerals (such as single-domain magnetite) have magnetic coercivities up to 300 mT. Also, at measurement time a standard specimen holder was not available for this procedure and specimens were oriented less percisely by hand. Figure B.3 shows specimen orientations. ARM data is included on the accompanying compact disc.

Six specimens were so processed. Specimen 145-c2-a was measured three times to see if the data were repeatable. The results were not repeatable and the data proved inconclusive. ARM measurements were, therefore, not included in final analysis.

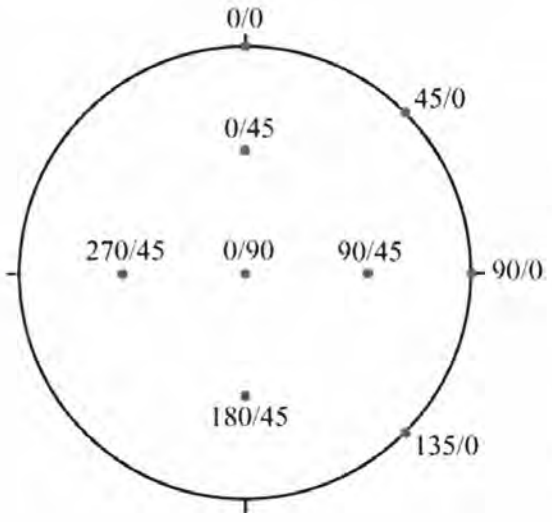

Figure B.3 Lower-hemisphere equal area projection of ARM orientations. The specimens were magnetized in each of these orientations and subsequently measured for remanence. The 0/90 position corresponds to the +z axis of a specimen, the 0/0 position corresponds to the +x axis of a specimen and the 90/0 position corresponds to the +y axis of a specimen.

Isothermal Remanent Magnetization (IRM)

IRM was measured to determine ferromagnetic mineral alignment. IRM was used in addition to ARM because the pulse magnetizer used (IM-10-30 Impulse Magnetizer) is capable of producing magnetic fields to 300+ mT. Therefore, it is able to magnetize single-domain magnetite. Limitations of this method include machinery and inability to demagnetize the specimen between magnetization steps. The Impulse Magnetizer operates by storing an electrical charge, and on operator command, discharging it thru a coil, which generates a magnetic field. However, it is up to an operator to trigger it, which leads to some uncertainty. Also, once specimens are magnetized at voltages relative to > 200 mT they cannot be demagnetized with the machinery available. So measurements might have components of remanence from previous magnetization steps. As of analysis time there was no equipment available to deal with these problems.

Three specimens were analyzed in this fashion. Data are included on the accompanying compact disc. Specimen 145-c2-a was analyzed three times with this method to determine if the IRM method was repeatable. Results showed that the IRM were not repeatable and, therefore, probably not valid. IRM data were not used in the final analysis.

Low Temperature Thermomagnetic Experiments in a Low Field

Another method used to determine what minerals contribute to the AMS was low temperature thermomagnetic experiments. Sixteen specimens were analyzed for bulk susceptibility changes as the specimens were slowly heated from –192°C (liquid nitrogen temperature) to 10°C (approximately room temperature). Data were acquired with the

Kappabridge CS-L. Specifications: accuracy of temperature sensor = ± 2°C, sensitivity to susceptibility changes = 1 x 10^{-7} (SI). The sixteen specimens were chosen to represent the range of susceptibility observed. Figure B.4 is a histogram of susceptibility for all the sites measured in the Cooper Mountain pluton. Included on the histogram are the number of sites per category and number of specimens measured in each category using low temperature thermomagnetics. Specimens were measured using the Kappabridge CS-3. Specifications: accuracy of temperature sensor = ± 2°C, sensitivity to susceptibility changes = 1 x 10^{-7} (SI). Calculations of the paramagnetic and ferromagnetic contributions to bulk susceptibility were made using equations from Hrouda (1994) and Hrouda et al. (1997). Results are listed in Table B.2. Eleven out of 16 specimens (69%) were dominated by paramagnetic contributions, four out of 16 specimens (25%) displayed bulk ferromagnetic susceptibility and one out of 16 (6%) showed paramagnetic and ferromagnetic contribution approximately equal. Example graphs of dominant paramagnetic versus ferromagnetic contributions are in Figure 9. Raw data are included on the accompanying compact disc.

For those sites with a non-paramagnetic AMS component, the magnetic fabric was similarly oriented to either magnetic or field fabric measurements from adjacent sites (see Figure 10). This suggests that the ferromagnetic minerals are oriented parallel to the paramagnetic ones.

Low Temperature Thermomagnetic Experiments in a High Field

The magnetic susceptibility of five specimens were measured in a high field at low temperatures to determine what minerals contribute to the anisotropy. Figure 11

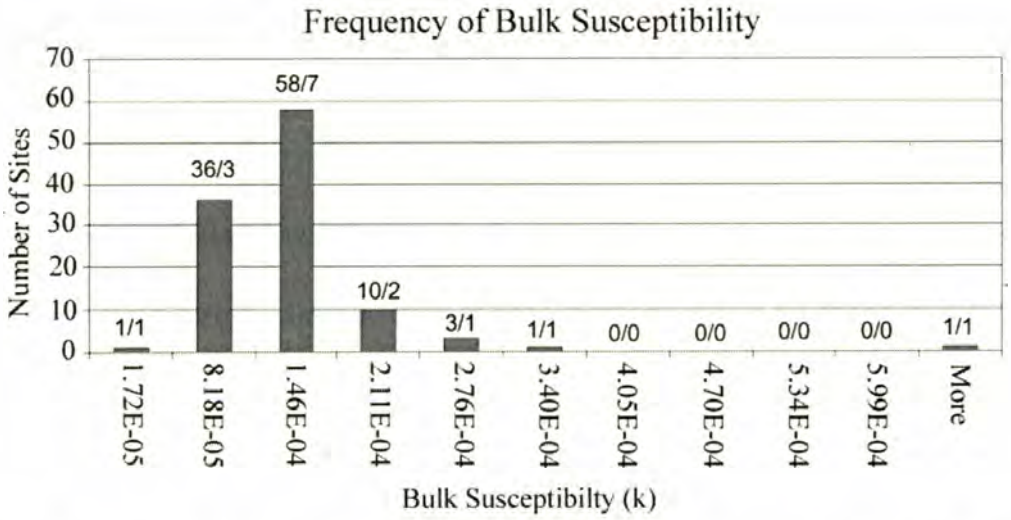

Figure B.4 Frequency of bulk susceptibility. This is a histogram of all the specimens used in the AMS study. Above each column is x/y; x = number of sites in each bulk susceptibility grouping, y = number of sites analyzed using low temperature thermomagnetic experiments in that grouping. See Table B.2 for low temperature thermomagnetic data.

Site	Sample		Hrouda (1994)				Hrouda et al. (1997)				Temp. range
Number	Number	Kt	Kp	Sp	Kf	Sf	Kp	Sp	Kf	Sf	calculated
188	124-c2-c	2.18	1.44	0.02	0.75	0.03	1.35	0.06	0.79	0.07	-190 to 0
214	143-c1-a	1.70	1.79	0.03	-0.09	0.04	2.31	0.08	-0.40	0.09	-190 to 0
304	204a-c1-a	0.29	0.86	0.01	0.43	0.02	0.62	0.04	0.58	0.05	-190 to 0
306	206-c1-a	1.21	1.10	0.01	0.11	0.12	0.91	0.04	0.22	0.05	-190 to 0
310	209b-c3-a	0.96	0.82	0.01	0.15	0.02	0.90	0.03	0.10	0.04	-190 to 0
366	247-c2-a	1.39	1.18	0.01	0.21	0.01	1.13	0.03	0.24	0.03	-190 to 0
373	254-c2-a	1.70	1.95	0.01	-0.25	0.02	2.23	0.02	-0.42	0.03	-190 to 0
378	259-c1-a	0.94	0.47	0.01	0.46	0.01	0.38	0.03	0.53	0.04	-180 to 0
101	68-c2-c	1.18	0.26	0.02	0.92	0.03	0.13	0.09	1.03	0.10	-150 to 0
127	88-c1-a	3.41	1.16	0.02	2.25	0.03	1.97	0.09	1.59	0.10	-150 to 0
179	117-c1-d	0.92	1.31	0.01	-0.39	0.02	1.55	0.04	-0.53	0.04	-192 to 0
305	205-c1-d	1.30	2.08	0.01	-0.78	0.03	2.51	0.04	-1.02	0.04	-192 to 0
325	219a-c1-a	0.55	0.83	0.01	-0.28	0.01	0.90	0.03	-0.32	0.03	-192 to 0
360	241-c3-a	3.00	1.11	0.01	1.89	0.03	0.67	0.04	2.13	0.04	-192 to 0
364	245-c1-a	0.91	1.29	0.01	-0.38	0.02	1.61	0.02	-0.56	0.03	-192 to 0
76	50-c1-a	4.71	1.34	0.02	3.37	0.03	2.02	0.12	2.82	0.14	-140 to -10

Table B.2 Low temperature thermomagnetic data. Kt = total susceptibility, Kp = paramagnetic contribution to susceptibility, Sp = paramagnetic contribution error, Kf = ferromagnetic contribution to susceptibility, Sf = ferromagnetic contribution error. Calculations made using equations from Hrouda (1994) and Hrouda et al. (1997).

shows an example of a specimen using this technique. The specimen is first cooled to 20 K and then it is slowly warmed to 300 K while the magnetic susceptibility is measured in a zero-field environment every five or ten degrees (lower curve in Figure 11). The specimen is then cooled and warmed again, but now the susceptibility is measured in a 2.5 T magnetic field (upper curve in Figure 11). An increase in susceptibility at temperatures below 120 K is due to single-domain magnetite (Dunlop and Özdemir 1997). Data files are on the accompanying compact disc.

Hysteresis Loops

The final technique used to determine minerals contributing to anisotropy was to acquire hysteresis loops. Eight specimens were magnetized to saturation magnetization in order to determine if the magnetite grains present were multi-domain or single-domain. Seven of the eight showed straight lines (no ferromagnetic minerals present) and only one specimen (specimen number 183-204a) contained multi-domain magnetite. This specimen reached saturation magnetization by 100 mT (0.1 T). Data files are the accompanying compact disc.

APPENDIX C

PALEOMAGNETISM

Paleomagnetism is magnetization in rocks that was acquired at some time in the past. Paleomagnetic methods measure the magnetic direction of minerals in a specimen. From that direction, a paleomagnetic pole for a body of rock can be determined. If the magnetic direction for the specimen is different from the direction expected for that age of magnetization and location, then something had to have happened to reorient the body of rock since its magnetization was acquired. The following is a description of procedures and lists of the data for the paleomagnetic study on the Cooper Mountain pluton.

SAMPLE COLLECTION

Oriented hand samples were collected for an AMS study and cores were drilled from those hand samples in the lab. Because the hand samples were originally collected for an AMS study, an average of two cores was drilled for each site. Only one specimen per site was used. Criteria for determining specimens: directions for components and maximum angular deviation (MAD) were obtained with principal component analysis (Kirschvink 1980), specimens with MAD greater than eight were filtered out, then multiple-specimen sites were reduced to one specimen by choosing a high N (number of points on a line-fit or plane-fit) or by comparing angle to origin to MAD. The specimens are listed in Tables 1 and 2.

THERMAL DEMAGNETIZATION

Over 90 sites were analyzed in this study. Data are listed in Tables 1 and 2. Raw data are included by site in the *.dat* and *.ngu* files on the accompanying compact disc.

Specimens were thermally demagnetized using an RFB-2 oven. The magnetic remanence for each specimen was measured with a cryogenic magnetometer. The accuracy of the cryogenic magnetometer is $\pm$ 1.99 x 10^{-11} Am^{-2} (based on the standard deviation of magnetic moments measured for an empty specimen holder ten times).

MAGNETIC VECTOR COMPONENTS

Two magnetic directions were resolved from the demagnetization paths. Discussion of these directions is in Chapter 1. Line-fit data are included in the *.gsl* files on the accompanying compact disc. These files are compatible with program IAPD.

WHAT MAGNETIC MINERALS CARRY THE REMANENCE?

It is helpful to know what magnetic minerals carry the remanence because it can reveal something about the temperature at which the remanence was acquired and possibly help to decipher to geologic history of the body of rock in question. Looking at the unblocking temperatures of the magnetizations can provide a simple answer. The unblocking temperature is the demagnetization temperature at which a specimen loses most of its magnetization. There were two groups of unblocking temperatures for specimens in the Cooper Mountain pluton. The high unblocking temperature, ~580°C, corresponded to the Curie temperature of magnetite. However, the ~370°C unblocking temperature was more anomalous. Blocking temperatures in the 370°C range suggest the

presence of pyrrhotite or titanomagnetite. High temperature thermomagnetic experiments were conducted to determine what magnetic minerals were present.

High temperature thermomagnetic experiments measure bulk magnetic susceptibility above room temperature. The temperature at which a specimen loses most of its susceptibility directly corresponds to its Curie temperature, which is characteristic for each magnetic mineral. For example, the Curie temperature of magnetite is 580°C, pyrrhotite is ~320°C and titanomagnetite has a large Curie temperature range (-150°C to 580°C) determined by titanium content. The specimens were measured with the Kappabridge CS-L. Specifications: field intensity = 300 Am^{-1}, sensitivity = 3 x 10^{-8} (SI) (for bulk susceptibility). A constant flow of argon at 60 mL/min was run through the specimen to provide a low-oxygen environment so that the specimen would not oxidize and new magnetic minerals would not be created. Data are included on the accompanying compact disc. High temperature thermomagnetic experiments showed magnetite as the only remanence-carrying mineral present (see Figure 14). This is consistent with reflected light microscopy (see Appendix A). See Chapter 1 for interpretation of mineral content. Examples of high and low unblocking temperature specimens are in Figure 14.

The Lowrie method (Lowrie 1990) of demagnetization was then used to further investigate a possible pyrrhotite component. The RFB-2 oven and cryogenic magnetometer were used in this evaluation. See the "Thermal Demagnetization" section of this appendix for the specifications of these two instruments. Explanation of the procedure is provided in Chapter 1 and raw data are included on the accompanying compact disc.